The Astrophysical Journal, 959:107 (20pp), 2023 December 20 https://doi.org/10.3847/1538-4357/ad004d

The Close AGN Reference Survey (CARS): An Interplay between Radio Jets and AGN Radiation in the Radio-quiet AGN HE0040-1105

M. Singha[1,2,3,4], N. Winkel[5], S. Vaddi[6], M. Perez Torres[7,8,9], M. Gaspari[10], I. Smirnova-Pinchukova[5], C. P. O'Dea[4], F. Combes[11], Osase Omoruyi[12], T. Rose[13,14], R. McElroy[15], B. Husemann[5], T. A. Davis[16], S. A. Baum[4], C. Lawlor-Forsyth[13,14], J. Neumann[5], and G. R. Tremblay[12]
[1] Astrophysics Science Division, NASA Goddard Space Flight Center, Greenbelt, MD 20771, USA; singham@myumanitoba.ca
[2] Department of Physics, The Catholic University of America, Washington, DC 20064, USA
[3] Center for Research and Exploration in Space Science and Technology, NASA Goddard Space Flight Center, Greenbelt, MD 20771, USA
[4] Department of Physics & Astronomy, University of Manitoba, 30A Sifton Road, Winnipeg, MB R3T 2N2, Canada
[5] Max-Planck-Institut für Astronomie, Königstuhl 17, D-69117 Heidelberg, Germany
[6] Arecibo Observatory, NAIC, HC3 Box 53995, Arecibo, Puerto Rico, PR 00612, USA
[7] Instituto de Astrofísica de Andalucía (IAA-CSIC), Glorieta de la Astronomía s/n, E-18008 Granada, Spain
[8] Facultad de Ciencias, Universidad de Zaragoza, Pedro Cerbuna 12, E-50009 Zaragoza, Spain
[9] School of Sciences, European University Cyprus, Diogenes Street, Engomi, 1516 Nicosia, Cyprus
[10] Department of Astrophysical Sciences, Princeton University, 4 Ivy Lane, Princeton, NJ 08544-1001, USA
[11] LERMA, Observatoire de Paris, PSL Research Université, College de France, CNRS, Sorbonne Université, UPMC, Paris, France
[12] Center for Astrophysics | Harvard & Smithsonian, 60 Garden Street, Cambridge, MA 02138, USA
[13] Department of Physics and Astronomy, University of Waterloo, Waterloo, ON N2L 3G1, Canada
[14] Waterloo Centre for Astrophysics, University of Waterloo, Waterloo, ON N2L 3G1, Canada
[15] School of Mathematics and Physics, University of Queensland, St Lucia, QLD 4072, Australia
[16] Cardiff Hub for Astrophysics Research & Technology, School of Physics & Astronomy, Cardiff University, The Parade, Cardiff CF24 3AA, UK
Received 2022 April 29; revised 2023 September 21; accepted 2023 September 21; published 2023 December 12

Abstract

We present a case study of HE 0040-1105, an unobscured radio-quiet active galactic nucleus (AGN) at a high accretion rate of $\lambda_{\rm Edd} = 0.19 \pm 0.04$. This particular AGN hosts an ionized gas outflow with the largest spatial offset from its nucleus compared to all other AGNs in the Close AGN Reference Survey. By combining multiwavelength observations from the Very Large Telescope/MUSE, Hubble Space Telescope/Wide Field Camera 3, Very Large Array, and European VLBI Network, we probe the ionization conditions, gas kinematics, and radio emission from host galaxy scales to the central few parsecs. We detect four kinematically distinct components, one of which is a spatially unresolved AGN-driven outflow located within the central 500 pc, where it locally dominates the interstellar medium conditions. Its velocity is too low to escape the host galaxy's gravitational potential, and may be re-accreted onto the central black hole via chaotic cold accretion. We detect compact radio emission in HE 0040-1105 within the region covered by the outflow, varying on a timescale of ∼20 yr. We show that neither AGN coronal emission nor star formation processes wholly explain the radio morphology/spectrum. The spatial alignment between the outflowing ionized gas and the radio continuum emission on 100 pc scales is consistent with a weak jet morphology rather than diffuse radio emission produced by AGN winds. >90% of the outflowing ionized gas emission originates from the central 100 pc, within which the ionizing luminosity of the outflow is comparable to the mechanical power of the radio jet. Although radio jets might primarily drive the outflow in HE 0040-1105, radiation pressure from the AGN may contribute to this process.

Unified Astronomy Thesaurus concepts: AGN host galaxies (2017); Radio jets (1347); Quasars (1319); Galaxy evolution (594)

1. Introduction

Active galactic nuclei (AGN) are capable of expelling ionized gas from the centers of galaxies with velocities that reach several hundred to tens of thousands of kilometers per second through a process known as AGN-driven outflows. Resolving the underlying physical processes behind these outflows is crucial for understanding galaxy evolution, as they are required to explain how AGN feed the energy from accreted materials back to their host galaxies (Fabian 2012; Gaspari et al. 2020; Hardcastle & Croston 2020), and produce tight positive correlations between the supermassive black hole (SMBH) mass and host galaxy properties (e.g., Silk & Rees 1998; King 2005; Kormendy & Ho 2013; Gaspari et al. 2019). Important questions that need to be resolved include how outflows are launched from the parsec-scale central engine, how they propagate through the host galaxy to reach kiloparsec scales, and how their energy thereby couples to the surrounding interstellar medium (ISM).

Outflows in the warm, ionized gas phase can be traced by the broad blueshifted wing components in the forbidden [O III] emission line doublet and are often detected in AGN (Cresci et al. 2015; Bischetti et al. 2017; Singha et al. 2021a). The statistical power of 1D optical spectroscopic data sets of large sky surveys has helped quantify their abundance and energetics. The spatial scales are particularly important to consider, as recent studies have shown that in many cases the luminous [O III]-emitting outflow is more compact than

expected (e.g., Husemann et al. 2016; Singha et al. 2022; Winkel et al. 2023). Spatially resolving the ionized gas outflow is therefore crucial to understanding the local impact on the host galaxy. Moreover, the nuclear outflow launching mechanism and the connection to the AGN phase remain elusive.

One scenario has been suggested, where ionized gas outflows are launched from parsec scales by the radiation pressure from the AGN accretion disk. Woo et al. (2016) and Rakshit & Woo (2018) found that the incidence of ionized gas outflows is predominantly correlated with the bolometric luminosity of AGN, which suggests that radiation pressure is the main driver of outflows. A recent work by Singha et al. (2021a) that focused on weakly accreting (Eddington ratio $\lambda_{\rm Edd} < 0.01$), low-excitation radio AGN (LERGs) also hinted at radiation pressure from the AGN accretion disk driving subkiloparsec-scale ionized gas outflows. The foundation for an AGN-wind scenario comes from numerous theoretical studies (Elvis 2000; King 2005; Proga 2007; Faucher-Giguère & Quataert 2012), followed by observations (Zakamska & Greene 2014; Baron & Netzer 2019; Sun et al. 2019; U et al 2022). They describe the momentum transfer from AGN-driven winds as the underlying physical mechanism that allows the ionized gas to expand. Theoretical studies such as those by King (2003) and Faucher-Giguère & Quataert (2012) found that the high-velocity wind-driven outflows were energy-conserving on large scales but momentum-conserving near their launch locations.

In recent years, several studies have suggested a possible connection between compact radio jets and multi-phase gas outflows. Studies by Whittle (1992), Tadhunter et al. (2003), Holt et al. (2008), and Morganti et al. (2013) suggested that the mechanical energy of compact radio jets could strongly perturb and accelerate the ambient multi-phase gas, creating bipolar outflows extended on subkiloparsec scales. Mullaney et al. (2013) and Molyneux et al. (2019) reported that compact radio jets could strongly interact with the ambient gas, resulting in a large line width of [O III]-emitting ionized gas clouds, $\mathrm{FWHM}_{[\mathrm{O\,III}]} > 1000\,\mathrm{km\,s^{-1}}$, originating from turbulent outflowing gas. This turbulence is a key element in the recurrent cycle of AGN feedback and feeding, in particular further stimulating the chaotic cold accretion (CCA) rain of multi-phase gas at different scales (e.g., Gaspari et al. 2018), thus inducing spectral line broadening.

It is clear that radio jets can shock, accelerate, and entrain the ambient gas in radio-loud AGN (Baum et al. 1997; Emonts et al. 2005; Laing & Bridle 2014; Mahony et al. 2016; Schulz et al. 2018), although the exact role of jets in radio-quiet AGN remains unclear. For a review of jets in radio-quiet AGN and their role in feedback see Singha et al. (2023). Unlike radio-loud AGN, radio-quiet AGN, which lack the kiloparsec-scale extended radio jet emission, constitute ∼90% of the AGN population. However, radio interferometric observations by Miller et al. (1993), Ulvestad et al. (2005), Gallimore et al. (2006), and Berton et al. (2020) showed that compact radio jets are present on subkiloparsec scales even in radio-quiet AGN.

Panessa et al. (2019) discussed different mechanisms of radio emission, which include star formation and the associated supernovae feedback, black hole coronal emission, AGN winds, and radio jets. Laor & Behar (2008) argued that processes induced by the magnetic field in the AGN corona, which causes nonthermal synchrotron emission, can create ionized gas outflows. In contrast, Blundell & Beasley (1998) proposed the observed radio emission in radio-quiet AGN is due to the thermal free–free emission from radiatively driven AGN winds. Zakamska & Greene (2014) reported that the shock-accelerated electrons by the AGN winds cause synchrotron emission. Aalto et al. (2017), Husemann et al. (2019), Jarvis et al. (2019), and Girdhar et al. (2022) suggested that small-scale radio jets could drive multi-phase gas outflows in radio-quiet AGN. The diversity of these mechanisms demonstrates the complexity of understanding the launching mechanism in radio-quiet AGN. Nevertheless, these results emphasize that small scales close to the nucleus must be probed to distinguish between the different mechanisms. Thus, spatially resolved multiwavelength observations of AGN-driven outflows are crucial to determining their properties in detail and identifying their powering mechanisms (e.g., Cicone et al. 2018).

The Close AGN Reference Survey[17] (CARS; Husemann et al. 2017; McElroy et al. 2022) consists of a sample of 40 unobscured, radio-quiet AGN, which well represents the majority of the nearby ($z < 0.06$) and luminous ($L_{\rm bol} < 10^{46}\,\mathrm{erg\,s^{-1}}$) AGN population. Singha et al. (2022) showed that the majority (63%) of the CARS sample, which have ionized gas outflows in the [O III] (blue wing), are spatially unresolved, and their flux-weighted centroids are located within 100 pc from the AGN nucleus. Moreover, the authors found that the occurrence of kiloparsec-scale outflows is not correlated with $L_{\rm bol}$, indicating that the radio emission or outflow timescales affect the outflows. An unambiguous understanding of the connection between radio emission and ionized gas outflows can only be made by spatially resolving both the radio and ionized gas emission on subkiloparsec scales.

In this work, we carry out a pilot study of HE 0040-1105 (R.A. = 00:42:36.9, decl. = −10:49:22; Husemann et al. 2022), a nearby ($z = 0.04196$), luminous ($L_{\rm bol} \sim 10^{44}\,\mathrm{erg\,s^{-1}}$) Seyfert 1 galaxy that hosts a radio-quiet, unobscured AGN. Due to its proximity (angular distance $D_{\rm A} \sim 171$ Mpc), HE 0040-1105 gives us a detailed view of the AGN–host galaxy interaction at a high spatial resolution where 1″ corresponds to 828 pc in the galaxy system. The host galaxy is an unbarred bulge-dominated galaxy with $M_{\rm B} = -19.38$ mag and a stellar mass of $\log(M_*/M_\odot) = 10.16^{+0.13}_{-0.10}$. Soft X-ray emission has been detected by ROSAT within the 0.1–2.4 keV range as well, with $f_{0.1\text{–}2.4\,\mathrm{keV}} = (7.36 \pm 0.81) \times 10^{-12}\,\mathrm{erg\,s^{-1}\,cm^{-2}}$ (Husemann et al. 2022).

HE 0040-1105's [O III] wing component is spatially unresolved at the resolution of the Very Large Telescope (VLT)/MUSE and the flux-weighted centroid of the blue wing [O III] is ∼90 pc offset from the nucleus (Singha et al. 2022), which represents the largest offset among the CARS AGN with unresolved outflows. By combining the 3D spectroscopic data with radio interferometric observations, we aim to trace the kinematic and spatial components of the outflow and discuss its potential origin.

This paper is organized as follows: in Section 2, we first briefly describe our observations and data reduction. We then investigate the ionized gas properties and radio emission in Section 3, while in Section 4 we attempt to explain the origin of any observed radio emission mechanisms and their potential connection to the outflows. We also discuss the ionization

[17] https://www.cars-survey.org

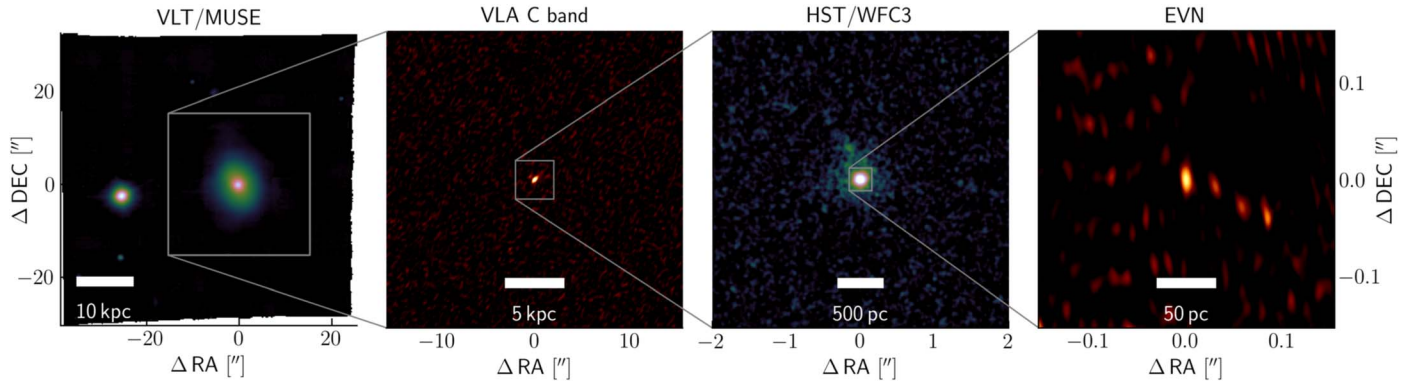

Figure 1. Overview of the data sets and their spatial coverage. From left to right the panels show the FoV of VLT/MUSE, VLA, a zoom-in onto the nucleus in the HST/WFC3 UVIS F225W image, and the EVN image. While the MUSE and VLA observations cover a large fraction of the host galaxy, HST allows a zoom into the central few 100 pc of the galaxy. The radio interferometry from EVN ultimately resolves the innermost few 10 pc near the AGN. The object 25″ east of HE 0040-1105 is a foreground star.

Table 1
Summary of Observational Characteristics and Depth

Band	Instrument	FoV	Sampling	Beam	t_{exp}	1σ Limit
Hα	VLT/MUSE	1′×1′	0.″2	0.″66 × 0.″66	800 s	5×10^{-18} erg s^{-1} cm^{-2} arcsec^{-2}
[O III]	VLT/MUSE	1′×1′	0.″2	0.″74 × 0.″74	800 s	7.5×10^{-18} erg s^{-1} cm^{-2} arcsec^{-2}
NUV	WFC3/UVIS F336W	40 ″×40 ″	0.″04	0.″07	696 s	1.29×10^{-18}erg cm^{-2} Å^{-1}e$-^{-1}$
C	VLA (A config)	4.′5	0.″066	0.″53 × 0.″27	1 hr	5.9 μJy beam^{-1}
X	VLA (A config)	4.′5	0.″033	0.″26 × 0.″17	1 hr	7.3 μJy beam^{-1}
L	EVN	9.″9	0.″0006	0.″02 × 0.″01	7 hr	12.05 μJy beam^{-1}

Note. VLT/MUSE provides IFU spectroscopy at 1″ resolution between 4800 and 9300 Å, covering a 1′ × 1′ region. VLA has a field of view (FoV) that is very similar to that of MUSE but is capable of imaging at 400 and 200 mas resolution between 4 and 8 GHz and 8 and 12 GHz. EVN resolves the nuclear region of the galaxy at 10 mas resolution.

mechanism of the emission line gas clouds. Finally, in Section 5, we present our conclusions.

We define the spectral index α as $S_\nu \propto \nu^\alpha$, where S_ν is the flux density and ν is the frequency. Throughout this paper, we adopt the standard flat Lambda cold dark matter cosmology with $H_0 = 70\,\mathrm{km\,s^{-1}\,Mpc^{-1}}$, $\Omega_m = 0.3$, and $\Omega_\Lambda = 0.7$.

2. Data

We utilize the CARS multiwavelength data set of HE 0040-1105 by combining the 3D spectroscopic optical cubes acquired with VLT/MUSE with radio observations obtained with the Very Large Array (VLA) and European VLBI Network (EVN). In this section, we briefly describe the observations and the data reduction procedures. We also summarize the multiwavelength observations in Table 1.

2.1. Optical Integral Field Spectroscopy

The CARS sample is exclusively selected on the *B*-band flux published in the Hamburg-ESO Survey (Wisotzki et al. 2000). It is designed such that it covers a representative sample of unobscured luminous AGN at redshifts $0.01 < z < 0.06$. As part of CARS, we obtained integral field spectroscopic observations of HE 0040-1105 with VLT/MUSE in the wide field mode (WFM; Husemann et al. 2017, 2022). The total integration time for HE 0040-1105 was 800 s with an effective seeing of ∼0.″62. All data were reduced with the standard ESO MUSE pipeline (Weilbacher et al. 2020) as described in Husemann et al. (2019) and Husemann et al. (2022). The first visual impression of the reduced data is given in Figure 1, where we show a broadband image constructed from the three-dimensional cube. We adopt the model of the stellar continuum emission of the host galaxy retrieved with the stellar population synthesis code `PyParadise`.[18] To analyze the spatially resolved host galaxy stellar and ionized gas component in Sections 3.1 and 3.3, we employ the stellar continuum subtracted reduced MUSE cube from CARS data release 1 (DR1; Husemann et al. 2022).

2.2. Near-UV Imaging

Near-UV (NUV) imaging was undertaken using the Wide Field Camera 3 (WFC3) on board the Hubble Space Telescope (HST) as part of the Cycle 28 GO program 16173 (PI: G. R. Tremblay; O. Omoruyi et al. 2023 in preparation). We imaged the target using the UVIS detector with the F225W and F336W filters (centered on rest-frame central wavelengths of $\lambda = 2358$ and 3354 Å, respectively) for 696 s (roughly half an orbital visibility) per filter. A six-point dither pattern was used to both optimally sample and avoid saturation of the point spread function (PSF) from the bright point source associated with the AGN. This PSF has not been subtracted from the images shown in this paper, although careful PSF subtraction will be presented in a forthcoming paper by Omoruyi et al. We used the UVIS 1k subarray mode to improve the detector readout time and therefore maximize the integration time across the dither pattern. The final FoV of each image is therefore 40″ × 40″. The data shown here were reduced using the standard HST/WFC3 recalibration pipeline (Sahu 2021)

[18] https://github.com/brandherd/PyParadise

including CTE correction. The `AstroDrizzle` (Gonzaga et al. 2012) algorithm was used to drizzle the final image to a pixel scale of 0.″04 pixel^{-1} using a pixel droplet fraction of 0.8.

2.3. Radio Interferometric Observations

2.3.1. VLA Imaging

We acquired radio interferometric observations of HE 0040-1105 with VLA on 2017 January 7, and 2016 November 22, in the *C* (4–8 GHz) and *X* (8–12 GHz) bands, respectively (project: 16B-084, PI: M. Pérez Torres). The array was set to the A configuration with a maximum baseline of 36.2 km. In both bands, the on-source integration time was 608 s. We used 3C 48 to set the flux density scale and J0050-0929 as the phase calibrator. We reduced the data with the Common Astronomy Software Applications (CASA version 6.2.1.7; McMullin et al. 2007) and the CASA VLA pipelines before reconstructing the image using the `tclean` routine with Briggs weighting. The resulting beam sizes along the major axes are 0.″5 (*C* band) and 0.″3 (*X* band), which both have an elongation of 0.″5 with respect to the minor axes. The JVLA observations provide sub-arcsec resolution of the radio structures close to the AGN nucleus as shown in Figure 9.

2.3.2. European Very Long Baseline Interferometric Network Imaging

Very long baseline interferometric (VLBI) observations of HE 0040-1105's continuum emission were retrieved with the European VLBI Network (EVN) at 18 cm (project code: EP119, PI: M. Pérez Torres) on 2020 March 12, where 16 stations were used to acquire the observations (Jb, Wb, Ef, O8, Tr, Hh, Sv, Zc, Ir, Sr, Ro, Cm, Da, Kn, Pi, and De). The total exposure time was 7 hr with a data recording rate of 1024 Mbps (8×16 MHz sub-bands, full polarization, two-bit sampling). While J0050-0929 was used as a fringe finder, both J0039-0942 and J0050-0929 were used as phase calibrators. The observations were carried out in the phase-referencing mode where the telescopes were pointed at the target and the phase calibrator in repeated 5 minute cycles. During each cycle, 4 minutes were spent on the target.

The EVN data set was calibrated in the Astronomical Image Processing System (AIPS), a software package developed by the National Radio Astronomy Observatory following the standard EVN data reduction guide.[19] The calibration tables that contain parallactic angle a priori gain corrections were transferred from the EVN pipeline. Additionally, the flag and bandpass tables were also transferred to the data set. The ionospheric dispersive delays were corrected using the VLBATECR task. We performed fringe fitting and bandpass calibration using the fringe finder. Delays and rates were corrected by fringe fitting the data from the phase reference calibrators. The final calibrated target data was exported to DIFMAP for imaging, and the resulting final image was created using natural weighting. The rms of the cleaned image is 12 μJy beam^{-1} and the peak intensity is 83.7 μJy beam^{-1}.

3. Analysis and Results

We perform a detailed multiwavelength analysis to investigate the spatial and kinematic properties of the AGN-driven ionized gas outflow, its origin, and its potential effects on the host galaxy. In Section 3.1, we analyze the stellar kinematics and measure the host galaxy's systemic redshift. This will allow us to derive the kinematics and energetics of the ionized gas outflow in Section 3.2.3. In Section 3.3, we then focus on different features that are present in the spatially resolved extended emission line region (EELR) of HE 0040-1105. Finally, we analyze the radio interferometric observations in Section 3.4 to examine whether the processes that drive the ionized gas outflow are related to the resolved radio structures.

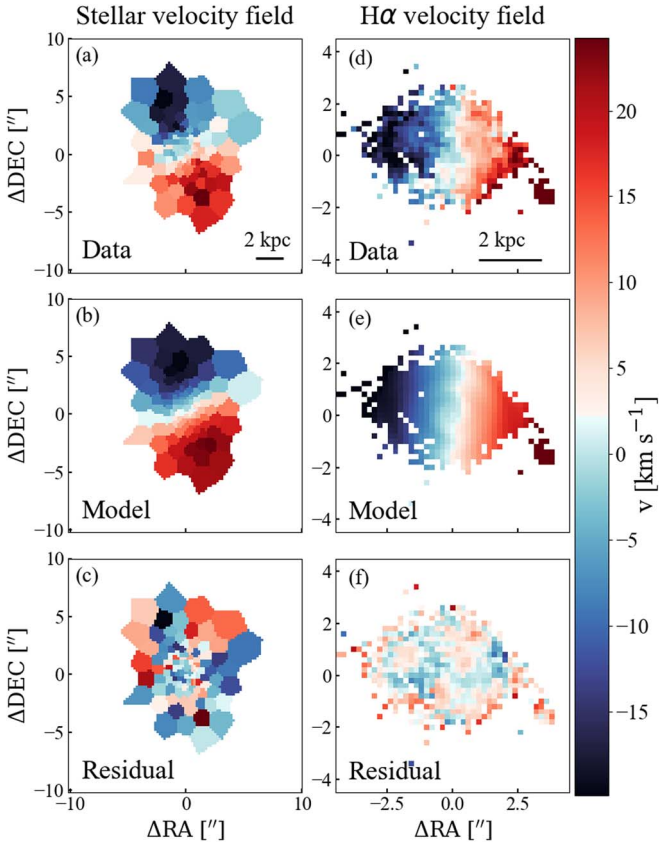

Figure 2. Kinematic modeling of HE 0040-1105's stellar (left columns) and Hα ionized gas (right columns) velocity field. From top to bottom, the panels show the velocities measured from the MUSE observations (see Sections 3.1 and 3.3.2), the tilted-ring model fitted to it, and the map with the residual velocities normalized by the uncertainty. In both cases, the thin rotating disk provides a good description of the velocity field, although the rotation axis between both host galaxy components is tilted by 53°.

3.1. Host Galaxy Stellar Component

To understand the dynamics of the ionized gas, we first need to constrain the kinematics of HE 0040-1105's stellar component. The stellar continuum model from CARS DR1 (Husemann et al. 2022; McElroy et al. 2022) allows us to map the stellar velocity field shown in the upper left-hand panel of Figure 2. We model the 2D velocity field with the tilted-ring model as described in Winkel et al. (2022). The code is based on the `KinMS` package (Davis et al. 2013), which was originally designed to simulate the atomic and molecular gas distributions of galaxies. We assume that the stellar emission originates from a rotating axisymmetric thin disk where the 2D line-of-sight velocity is described by

$$v_r = v_{sys} + v \sin(i)\cos(\phi + \mathrm{PA}), \quad (1)$$

[19] https://www.evlbi.org/evn-data-reduction-guide

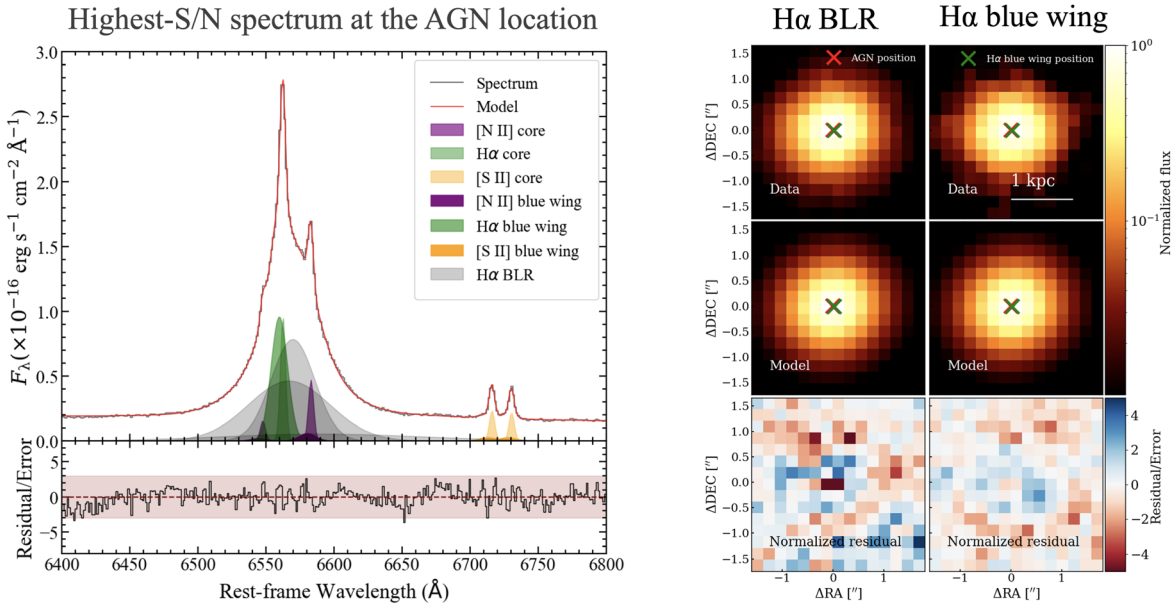

Figure 3. Spectroastrometric analysis of the Hα emission within the central $3'' \times 3''$ diameter region. The upper portion of the left panel shows the $3'' \times 3''$ spectrum (black continuous line) together with the multicomponent fit of the emission line spectrum (red continuous line) in the Hα + [N II] $\lambda\lambda$6548, 6583 window. The Gaussian components denoting Hα NLR emission are shown by the green-shaded regions. The purple-shaded Gaussian components represent the [N II] $\lambda\lambda$6548, 6583 emission lines, and the orange-shaded Gaussian components describe the [S II] $\lambda\lambda$6716, 6731 emission line doublets. We adopt light-colored shading for the narrow core and dark shading for the blue wing components. The gray-shaded Gaussian components define three broad-line region (BLR) Gaussians B_0, B_1, and B_2. The lower portion of the left panel shows the normalized residual spectrum (black line), which is contained in the 3σ region (shaded red) across the entire wavelength range, representing the residuals divided by the error spectra. The corresponding 2D light profiles Σ_{2D} of the Hα broad and wing components are shown in the right panels. From top to bottom, the panels describe the measured Σ_{2D} profile, the best-fit Moffat model, and the residual maps normalized by the uncertainty. The red cross describes the AGN location, whereas the green cross highlights the flux-weighted centroid of Σ_{2D}, i.e., the component's location. The corresponding error-normalized residual maps show no systematic substructures, implying that both the Hα broad and wing components are spatially unresolved.

where v_{sys} is the systemic velocity, PA is the position angle of the rotation axis, and ϕ is the azimuthal angle measured around the AGN position in the observed plane. We then use the `GAStimator` algorithm[20] to maximize the log-likelihood of the line-of-sight velocity distribution and radially evaluate the model in concentric aperture rings. For this step, we only adopt the bins where the uncertainty in the radial velocity is smaller than 10 km s^{-1}. Assuming a smooth rotation curve, we radially interpolate the parameters (v_{sys}, PA, ϕ) to generate the model for the 2D velocity field, which radially traces the rotation curve of the host galaxy stellar component.

In order to achieve a minimum signal-to-noise ratio (S/N) of ~ 20 of the stellar emission, we use the Voronoi tessellation technique (Cappellari & Copin 2003) and co-add spectra within cells. The stellar velocity field shows a smooth rotation curve and is largely unperturbed with a median PA $= 69° \pm 5°$. The rotation curve increases linearly from 4 km s^{-1} near the nucleus to 43 km s^{-1} at $4''$ (3.2 kpc) where it flattens. However, we note that the velocity near the center should be regarded as a lower limit due to beam smearing. Based on the best-fit model, we spatially map the velocity field with respect to the kinematic center of the disk-like rotation, that is HE 0040-1105's systemic velocity $v_{sys} = cz = 12583.2 \pm 0.5$ km s^{-1}, as shown in Figure 3. HE 0040-1105's median stellar velocity dispersion is $\sigma_* = 128 \pm 2$ km s^{-1}.

3.2. Nuclear Ionized Gas Outflow O1

An important feature that has already been identified in Singha et al. (2022) is the warm ionized gas outflow driven by the AGN with a size of 741 ± 3 mas. Although this outflow was identified from the Hβ + [O III] $\lambda\lambda$4959, 5007 + Fe II $\lambda\lambda$4923, 5018 emission line complex, it has a corresponding component in the Hα emission that has not yet been analyzed.

We first constrain this component's location with a similar approach as described in Singha et al. (2022) before we estimate the outflow integrated energetics and discuss its impact on the host galaxy.

3.2.1. Identifying the Outflowing Hα Component

We constrain the outflow properties by modeling its emission line spectrum with a superposition of multiple Gaussian components. For the AGN continuum, we use a linear model, which provides a sufficient description over the relatively narrow wavelength range analyzed. The broad component of the Hα emission line is considerably more complex than that of Hβ, so we require three components, B_0, B_1, and B_2, to describe the broad emission line profile.

The narrow Hα + [N II] $\lambda\lambda$6548, 6583 + [S II] $\lambda\lambda$6716, 6731 emission lines are robustly described by a linear superposition of kinematically coupled Gaussian components. We keep the line flux ratios for [N II] λ6548/[N II] λ6583 tied to their theoretical prediction of 1/3 (Storey & Zeippen 2000). To account for the outflow that manifests as a blue wing, we describe each of the lines with two Gaussian components—a first narrow *core* component that describes the ionized gas locally to the galaxy and a second broader *wing* component that represents the ionized gas outflow. These constraints allow us to achieve a robust fit for the emission lines.

We fit the spectrum extracted from the central brightest pixel using a nonlinear Levenberg–Marquardt algorithm and

[20] https://github.com/TimothyADavis/GAStimator

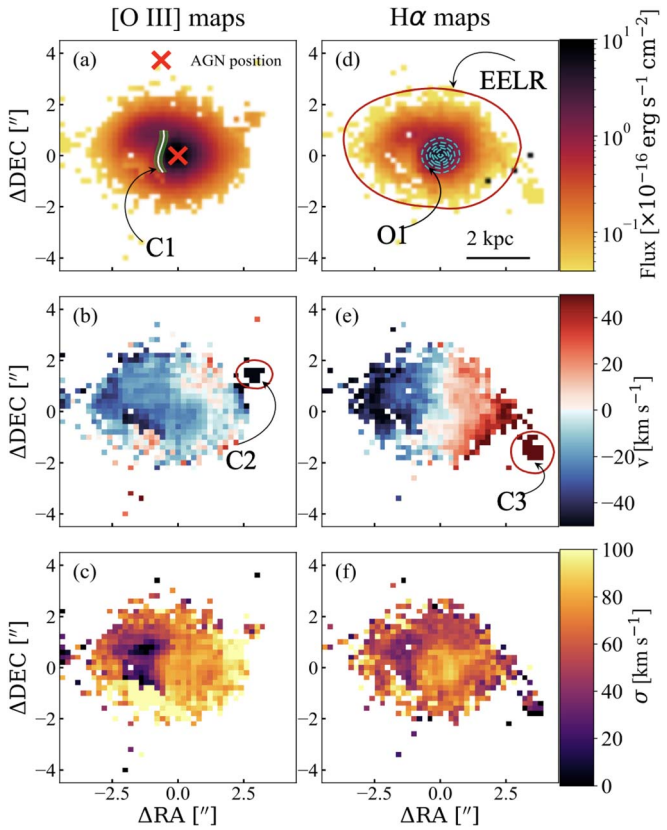

Figure 4. Mapping HE 0040-1105's ionized gas flux and kinematics across the host galaxy. The left panels show the maps extracted from the single-component [O III] model, and the right panels are those for Hα. From top to bottom, the panels show the emission line flux, rest-frame velocity v, and velocity dispersion σ, respectively. The EELR that is local to the galaxy (see Section 4.2.1) is highlighted by the red contour in panel (d). The contours of ionized gas outflow in the center (see Section 3.2) are shown as dashed cyan lines. In addition, we highlight the contours of the kinematic features analyzed in Section 3.3 where the red line in panel (b) describes the morphology of the receding shell C1, and the red line in panel (e) indicates the Hα emitting receding region C3. Both [O III] emission line nebulae have similar morphologies. However, while the Hα velocity field has a clear rotational pattern and a nucleated peak of the velocity dispersion, the [O III] shows a more chaotic motion with a velocity dispersion in C1 that is lower than average.

estimate the uncertainties by performing the fit for 100 mock spectra generated from the corresponding error spectrum.

To estimate whether multiple components are required, we use the Akaike information criterion (AIC; Akaike 1974) where we penalize the additional component if the value of $\mathrm{AIC_s} = 2\ln(L_s) + 2k_{fs}$ is greater than 40. Here, L_s represents the likelihood of the model and k_{fs} indicates the number of free parameters used by the model. Furthermore, we only adopt the additional outflow component if its S/N is greater than 5.

For the best-fit model, we find that the outflow component is relatively broad. Its width as quantified by the velocity range that contains 80% of the line flux is $W_{80,\mathrm{H}\alpha,\mathrm{wing}} > 400\ \mathrm{km\ s^{-1}}$, indicating that the outflow is driven by the AGN (Harrison et al. 2014; McElroy et al. 2015).

3.2.2. Size of the Ionized Gas Outflow

To spatially trace the 2D light distribution for the different kinematic components present in the Hα + [N II] + [S II] complex, we use a similar spectroastrometric approach to that described in Singha et al. (2022). We fix the kinematic parameters of the emission lines to those retrieved from the central brightest spectrum while only varying the line flux across the FoV. A significant difference from Singha et al. (2022); however, for the multiple broad components, we only keep the single-line flux of B_1 as a free parameter while keeping the line flux ratios B_0/B_1 and B_2/B_1 fixed to what we derived from the central spectrum. Fixing the line ratios is a sensible approach since the emission from the BLR is spatially unresolved.

After fitting each spaxel in the inner $3'' \times 3''$ with the compound model, we construct the 2D surface brightness profile Σ_{2D} for each of the individual emission lines. Since the high S/N broad emission is spatially unresolved, Σ_{2D} corresponds to the empirical PSF. We then fit the empirical PSF with a 2D Moffat model, as well as Σ_{2D} of the Hα blue wing ($\Sigma_{2D,\mathrm{H}\alpha,\mathrm{wing}}$). Following the procedures described in Singha et al. (2022), we find that the Moffat model well describes the $\Sigma_{2D,\mathrm{H}\alpha,\mathrm{wing}}$ profile, suggesting that the blue wing in Hα is spatially unresolved by MUSE. The empirical PSF extracted at Hα differs (FWHM = 656 mas) from that at Hβ (FWHM = 741 mas) because the line shape of the PSF varies with wavelength (Cypriano et al. 2010; Eriksen & Hoekstra 2018).

We estimate the statistical uncertainty of the astrometrically measured quantities using a Monte Carlo approach, similar to that described in Singha et al. (2022). We adopt the standard deviation of the distribution as the statistical uncertainty of the centroid location σ_{stat}. Furthermore, we estimate the systematic uncertainty of our spectroastrometric measurements $\sigma_{sys,cor}$ as described in Singha et al. (2022). In this way, we account for systematic effects on our 3D spectroscopic data set, including detector noise and the geometric distortion of the CCD. The total uncertainty adopted for the following analysis is $\sigma_{cor} = (\sigma_{stat}^2 + \sigma_{sys}^2)^{1/2}$.

The offsets between the flux-weighted centroids of the [O III] and Hα blue wings and the AGN nucleus in the kinematically perturbed region O1 (see Figure 4) are $d_{\mathrm{AGN}}^{[\mathrm{O\ III}],\mathrm{O1}} = 92 \pm 8$ pc and $d_{\mathrm{AGN}}^{\mathrm{H}\alpha,\mathrm{O1}} = 29 \pm 7$ pc. Constraining the size of this region is limited by the finite width of the MUSE PSF. Since their Σ_{2D} profiles are not resolved by MUSE, we estimate $\mathrm{FWHM}_{\mathrm{MUSE}}^{\mathrm{maj}}$, where we adopt the width of the elliptical PSF along the major axis as $\mathrm{FWHM}_{\mathrm{MUSE}}^{\mathrm{maj}} = 741 \pm 3$ mas (for Hβ) and 656 ± 3 mas (for Hα; Singha et al. 2022). If we assume that both the [O III] and Hα blue wings originate from the same intrinsic outflow O1, it is sensible to adopt the larger size of the PSF widths, which is the one measured at Hβ, to comprehend the maximum possible size of the region perturbed by the outflow. In coordinates of the galaxy system, the maximum projected radial distance of the outflow from the nucleus amounts to 308 pc.

We note that the derived offsets and sizes are prone to projection effects. The deprojected offsets could only be calculated if the inclination angle of the AGN nucleus i of HE 0040-1105 with respect to our line of sight is known. Since the outflow inclination of HE 0040-1105 is unconstrained, we can use the statistical estimate of the mean unobscured inclination of AGN described in Singha et al. (2022), $i_{\mathrm{mean}} = 40° \pm 2°$, which results in a maximum intrinsic outflow radius, $d_{\mathrm{max,intr}} = 308\ \mathrm{pc}/\sin(i) = 480$ pc.

For the following analysis, unless stated differently, we adopt the projected distances, which involve fewer assumptions on the geometry.

3.2.3. Outflow Energetics

We estimate the outflow energetics from the integrated flux from the ionized gas outflow O1. As a first step, we determine the outflowing ionized gas mass assuming "Case B" recombination with the Balmer decrement $H\alpha/H\beta = 2.86$ and an electron temperature of $T_e \approx 10^4$ K. Following Harrison et al. (2014), the ionized gas mass can be estimated as

$$\frac{M_{\rm ion}}{2.82 \times 10^9\, M_\odot} = \left(\frac{L_{H\beta,\,\rm O1}}{10^{43}\ {\rm erg\ s^{-1}}}\right)\left(\frac{n_{\rm e,O1}}{100\ {\rm cm^{-3}}}\right)^{-1}, \quad (2)$$

where $L_{H\beta,01}$ is the extinction-corrected luminosity in Hβ and $n_{\rm e,O1}$ the electron density for O1. We infer a line-of-sight attenuation from a Milky Way–like attenuation curve, following Cardelli et al. (1989). We estimate $A_{\rm V,O1} = 2.71 \pm 0.68$ mag, indicating significant dust extinction in the system O1. The extinction uncorrected Hβ luminosity in O1 is $\log(L_{H\beta,\,\rm O1,obs}/{\rm erg\ s^{-1}}) = 40.13 \pm 0.01$. We correct $L_{H\beta,\rm O1,obs}$ with the optical extinction and estimate the extinction-corrected Hβ luminosity as

$$L_{H\beta,\,\rm O1,int} = L_{H\beta,\,\rm O1,obs} \times 10^{A_{\rm V,O1}/2.5}. \quad (3)$$

$\log(L_{H\beta,\,\rm O1,int}{\rm erg\ s^{-1}})$ is estimated to be 41.21 ± 0.27, which yields $M_{\rm out} = (3.96 \pm 0.07) \times 10^6 M_\odot$.

The derived values of the energetics depend on the assumed geometry, which is unresolved in our IFU observations. To estimate the outflow energetics we therefore adopt geometries discussed in previous studies. A biconical outflow geometry has been used in several studies (e.g., Cano-Díaz et al. 2012; Cresci et al. 2015; Fiore et al. 2017) where the cones are homogeneously filled with gas. In this case, the mass outflow rate can be estimated from the outflow velocity $v_{\rm out}$ as

$$\frac{\dot{M}_{\rm ion,cone}}{M_\odot\ {\rm yr^{-1}}} = 3\left(\frac{v_{\rm out}}{100\ {\rm km\ s^{-1}}}\right)\left(\frac{M_{\rm ion}}{10^7\, M_\odot}\right)\left(\frac{R_{\rm out}}{\rm kpc}\right)^{-1}, \quad (4)$$

where $R_{\rm out}$ indicates the distance from the nucleus for which we adopt $d_{\rm max,intr} = 480$ pc, the deprojected maximum radius of the ionized gas outflow (see Section 3.2.2). We further estimate the momentum injection rate as $\dot{P}_{\rm ion} = \dot{M}_{\rm ion} v_{\rm out}$ and the kinetic energy injection rate as $\dot{E}_{\rm ion} = \dot{M}_{\rm ion} v^2/2$.

While the choice of $v_{\rm out}$ significantly affects $\dot{M}_{\rm ion,\,cone}$, past studies have assumed different parameterizations such as the velocity range of $W_{80}/1.3$ (Rupke & Veilleux 2013; Harrison et al. 2015; McElroy et al. 2015; Husemann et al. 2019), the radial velocity of the blue wing component, $v_{\rm broad}$, or the maximum velocity of the emission line gas, $v_{\rm max}$. To account for the systematic differences between the prescriptions, we compute the outflow energetics for each of them.

To test the impact of the assumed outflow geometry on the derived quantities, we now change to a shell-like geometric model. In this case, the mass outflow rate can be estimated following Husemann et al. (2019):

$$\frac{\dot{M}_{\rm out,\,shell}}{M_\odot\ {\rm yr^{-1}}} = \left(\frac{v_{\rm out}}{100\ {\rm km\ s^{-1}}}\right)\left(\frac{M_{\rm out}}{10^6\, M_\odot}\right)\left(\frac{100\ {\rm pc}}{\Delta R}\right), \quad (5)$$

where ΔR is the thickness of the shell. Husemann et al. (2019) estimated $\Delta R = 20$–500 pc for the shell thickness of an ionized gas outflow of 1 kpc extent. For HE 0040-1105, we have shown in Singha et al. (2022) that the outflow is located at less than

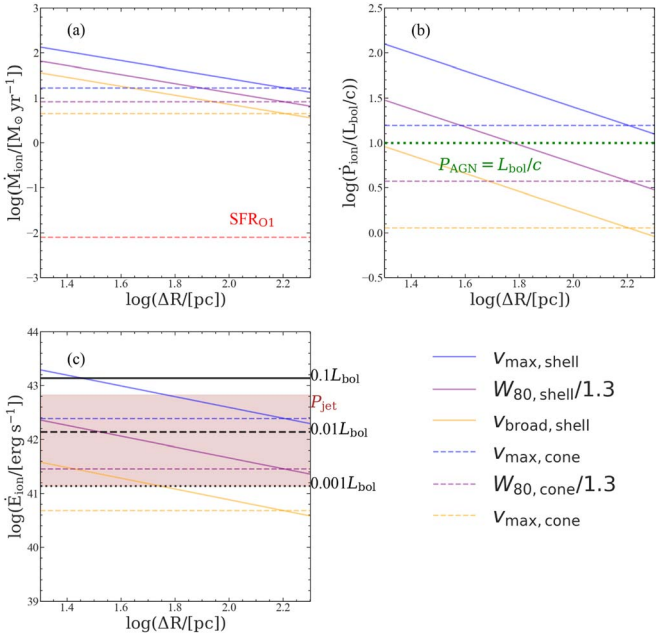

Figure 5. Outflow energetics parameters vs. the shell thickness for different $v_{\rm out}$ and different outflow geometries. (a) Mass outflow rates, (b) momentum injection rates, and (c) kinetic energy injection rates. The blue, purple, and yellow lines correspond to $v_{\rm out} = v_{\rm max}$, $W_{80}/1.3$, and $v_{\rm broad}$, respectively. We use solid lines to showcase the parameters derived for the shell geometry and dashed lines for the cone geometry. The red dashed line in (a) corresponds to the Hα-derived nuclear SFR. The green dotted line in (b) shows the momentum injection by the AGN radiation field, $P_{\rm AGN} = L_{\rm bol}/c$. The black lines in (c) show the 0.1% (dotted line), 1% (dashed line), and 10% (solid line) energy released from the AGN, respectively. The energy-driven mechanism is feasible. The brown-shaded region denotes the possible values of the jet power $P_{\rm jet}$.

<500 pc from the nucleus. Therefore, we show the injection rates of mass, momentum, and kinetic energy for $\Delta R = 20$–250 pc (reducing the upper limit on ΔR by a factor of 2) in Figure 5, and use $\Delta R = 100$ pc in Table 2.

The estimated $\dot{M}_{\rm ion}$ values for both geometries and for all velocities are at least an order of magnitude higher than those predicted from the AGN-wind scaling relations for ionized gas outflows by Fiore et al. (2017). The lower limit of $\dot{M}_{\rm ion}$ is close to the $\log(L_{\rm bol})$–$\dot{M}_{\rm ion}$ relation for the luminous quasars as shown in Singha et al. (2021a). The upper limit of $\dot{M}_{\rm ion}$ in HE 0040-1105 is about an order of magnitude higher than that expected from the scaling relation. However, its value is consistent with the $\dot{M}_{\rm ion}$ of LERGs at similar $L_{\rm bol}$, which are systems in which the radio source increases the mass loading (Singha et al. 2021a).

3.2.4. Star Formation Rate in O1

Star formation-related processes can inject momentum and energy into the ambient medium, which may be able to explain the observed ionized gas outflow signatures on several hundred-parsec scales. We now aim to estimate the integrated star formation rate (SFR) over the central 1″ aperture, to estimate whether nuclear star formation can drive the ionized gas outflow. Using the BPT diagnostic, we conclude that HE 0040-1105's warm gas component is predominantly ionized by the AGN (Smirnova-Pinchukova et al. 2022). From the Hα luminosity, we can therefore only estimate an upper limit for star formation. We first correct the Hα luminosity for dust extinction in the galaxy following Winkel et al. (2022),

Table 2
Derived Parameters for the Energetics of HE 0040-1105's Ionized Gas Outflow O1

	Cone Geometry			Shell Geometry		
	$\log(\dot{M}_{\rm out}/M_\odot\ {\rm yr}^{-1})$	$\log(\dot{P}_{\rm out}\,{\rm dyne}^{-1})$	$\log(\dot{E}_{\rm out}/{\rm erg\ s}^{-1})$	$\log(\dot{M}_{\rm out}/M_\odot\ {\rm yr}^{-1})$	$\log(\dot{P}_{\rm out}\,{\rm dyne}^{-1})$	$\log(\dot{E}_{\rm out}/{\rm erg\ s}^{-1})$
$v_{\rm broad}$	0.66	33.72	40.68	0.86	33.92	40.88
$W_{80}/1.3$	0.92	34.24	41.46	1.12	34.44	41.66
$v_{\rm max}$	1.23	34.86	42.39	1.43	35.06	42.59

Note. We compute the outflowing mass rate $\dot{M}_{\rm out}$, the momentum Injection rate $\dot{P}_{\rm out}$, and the kinetic energy injection rate $\dot{E}_{\rm out}$ for a cone geometry (left columns) and a shell-like geometry (right columns). The rows contain the values for the different parameterizations of the velocity. while the geometry only affects the 0.2 dex, the choice of the velocity can change the momentum and energy loading by more than one order of magnitude. We have not provided the uncertainties with these measurements as they are smaller than the scatter derived using different assumptions. The assumed velocity values are $v_{\rm broad} = -183\ {\rm km\ s}^{-1}$, $W_{80}/1.3 = 332\ {\rm km\ s}^{-1}$, and $v_{\rm max} = 680\ {\rm km\ s}^{-1}$.

Table 3
Kinematic Features Identified in HE 0040-1105's Ionized Gas Nebula and Their Properties

Name	Emission Lines	v (km s^{-1})	σ (km s^{-1})	W_{80} (km s^{-1})	$v_{\rm max}$ (km s^{-1})	$d_{\rm AGN}$ (kpc)	Resolved	Size (kpc)
O1	Hβ + [O III]	-183 ± 4	249 ± 3	432 ± 6	680 ± 7	0.092 ± 0.008	Yes	<0.307
	Hα + [N II] + [S II]	-135 ± 10	283 ± 12	566 ± 21	700 ± 26	0.028 ± 0.008		
C1	Hβ + [O III]	$+40 \pm 2$	132 ± 2	293 ± 7	304 ± 4	0.515	Yes	$<1.5 \times 0.26$
	Hα + [N II] + [S II]	$+69 \pm 31$	116 ± 15	278 ± 26	301 ± 42			
EELR	Hβ + [O III]	-90 – $+60$	0 – 120	0–310	40 – 320	…	Yes	$<2.8 \times 1.8$
	Hα + [N II] + [S II]	-60 – $+80$	0 – 120	0 – 310	10 – 310			
C2a	Hβ + [O III]	-224 ± 4	61 ± 3	156 ± 8	346 ± 7	2.6	no	<0.307
	Hα + [N II] + [S II]	-215 ± 5	71 ± 5	181 ± 35	356 ± 11			

Note. From left to right the columns contain the feature name, the emission line in which it is detected, the kinematic parameters velocity v, dispersion σ, line width W_{80}, and peak velocity $v_{\rm max}$, along with a distance to the central AGN $d_{\rm AGN}$, whether the feature is resolved or not, and the projected spatial size.

which yields an extinction-corrected luminosity of $\log(L_{{\rm int,H}\alpha}/{\rm erg\ s}^{-1}) = 39.18 \pm 0.17$. Then, we use the calibration of Calzetti et al. (2007) to convert it into an SFR of

$$\frac{\rm SFR}{M_\odot\ {\rm yr}^{-1}} = 5.3 \times 10^{-42}\left(\frac{L_{{\rm int,H}\alpha}}{\rm erg\ s^{-1}}\right), \quad (6)$$

where we find an upper limit of SFR of only $8 \times 10^{-3}\,M_\odot\ {\rm yr}^{-1}$ within the central $<1''$.

3.3. Spatially Resolved Ionized Gas

3.3.1. Single-component Emission Line Modeling

In order to analyze the resolved emission of ionized gases, we first subtract the unresolved emission from the original data cube. The unresolved emission consists of the BLR emission together with the spatially unresolved blue wing components that originate from the outflowing system O1. After subtracting pointlike emission, the 3D cubes span 4750–5090 and 6400–6800 Å and exclusively contain the unresolved host galaxy emission, including the contribution from the EELR.

We employ a simple single-component model to fit the emission line shape throughout the MUSE FoV to characterize the emission of HE 0040-1105's ionized gas component. Here, we independently model the emission line complexes Hβ + [O III] and Hα + [N II] + [S II] using a linear superposition of kinematically coupled Gaussian components. Similarly to Section 3.2.1, we fix the line ratios among the line doublets [O III] λ4959/[O III] λ5007 and [N II] λ6548/[N II] λ6583 to their theoretical prediction of 1/3.

We notice that the single-component model does not properly describe the emission line shapes in some regions of HE 0040-1105's ionized gas nebula. In regions where the line shape differs, we first constrain the kinematics of this structure by disentangling the low S/N components from the integrated spectra of multiple 3×3 spaxel apertures. After the kinematics are constrained, all spaxels are then independently fitted with the two-component model, and the AIC criterion described in Section 3.2.1 determines whether it provides a better description of the emission line shape than the single-component model. We find that the single-component model has a contribution across the entire FoV such that C2 corresponds to the local EELR of HE 0040-1105's host galaxy.

From both the spatial distribution of the ionized gas flux and the kinematic components present in their emission lines, we identify three additional features (C1, C2, and C3; see Figure 4) that are not associated with the local host galaxy EELR. Their kinematic properties, locations, and sizes are listed in Table 3. In the following, we characterize them, along with the EELR, in more detail.

3.3.2. The EELR Local to the Host Galaxy

The EELR is spatially resolved by MUSE and this large ionized gas nebula extends up to a distance of ∼2.8 kpc from

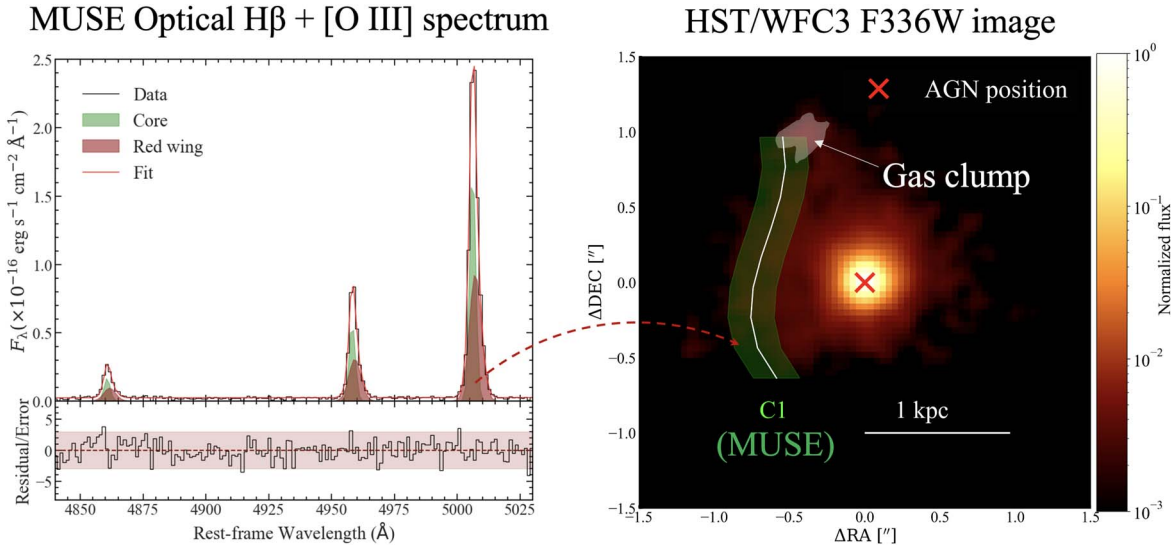

Figure 6. Multiwavelength view of region C1. Left panel: MUSE optical spectra extracted from a 3 × 3 spaxel region (in gray), along with its multi-Gaussian component fit (in red). The green-shaded Gaussian components represent the narrow core, which is a part of the EELR, whereas the dark brown-shaded components trace the red-wing component, corresponding to region C1. Right panel: HST/WFC3 near-UV image centered at 3350 Å. The green region describes the area covered by the deconvolved C1, and the white line denotes its centroids. A clumpy structure on the northeastern side of the nucleus is shaded with white to showcase its spatial location and morphology. C1 overlaps with the gas clumps on the north where S/N > 5. Such spatial coincidence indicates that C1 is a part of the clumpy region.

the central nucleus. In Figure 4, we show the 2D flux and kinematic profiles for the ionized gas in [O III] and Hα.

On the northeastern side of the nucleus, the [O III] emitting gas clouds appear blueshifted, with a median radial velocity of $v_{[\mathrm{O\ III}],\mathrm{EELR}} = -25 \pm 3\ \mathrm{km\ s^{-1}}$ that remains uniform up to the outer boundary of the nebula (Figure 4(b)). We notice that the [O III] velocity dispersion, $\sigma_{[\mathrm{O\ III}],\mathrm{EELR}}$ decreases by $<20\ \mathrm{km\ s^{-1}}$ where C1 is located (Figure 4(c)). On the other hand, the radial velocity ($v_{\mathrm{H}\alpha,\mathrm{EELR}}$) profile of the H$\alpha$ clouds shows a relatively smooth velocity gradient from the eastern side to the western side (Figure 4(e)). No significant decrease in their dispersion $\sigma_{\mathrm{H}\alpha,\ \mathrm{EELR}}$ is observed at the location of C1, where the median is $\sigma_{\mathrm{H}\alpha,\ \mathrm{EELR}} = 35 \pm 7\ \mathrm{km\ s^{-1}}$ (Figure 4(f)). The gas kinematics in the EELR is thus quiescent, in contrast with O1.

Nelson & Whittle (1996) observed a tight correlation between $\sigma_{[\mathrm{O\ III}]}$ and σ_*, suggesting that the kinematics of the EELR gas in Seyfert galaxies is controlled by the bulge gravitational potential. Studies by Greene & Ho (2005) and Bian et al. (2006) also found that the median ratios between the velocity dispersion of ionized gas and stars ($r_{\mathrm{ion}/*} = 1.00 \pm 0.35$, and 1.20 ± 0.96, respectively) confirm the bulge-dominated gravitational motion on kiloparsec scales. The median $r_{\mathrm{ion}/*}$ in the EELR, $r_{\mathrm{ion}/*,\mathrm{EELR}} = 0.58 \pm 0.22$, implying that the EELR gas in HE 0040-1105 is sub-virial, and hence cannot escape the bulge potential of the host.

3.3.3. EELR Kinematic Modeling

Similar to the stellar velocity field, we fit the kinematic modeling of the 2D radial velocity profile Hα ionized gas velocity field with a tilted-ring model as described in Section 3.1. We obtain a robust fit where the small residuals scatter around the rest-frame velocity of the host galaxy. Between the concentric rings, we find a median PA of $16 \pm 2°$. The $v_{\mathrm{H}\alpha}$ profile of the EELR is well described by a thin rotating disk model, as shown in Figure 2. We find the difference in PA between the stars and the ionized gas to be $\mathrm{PA}_{\mathrm{star-gas}} = 53° \pm 2°$. The quiescent kinematics of the ionized gas in the EELR and the significant $\mathrm{PA}_{\mathrm{star-gas}}$ are indicative of the external origin of gas in HE 0040-1105, such as early, ongoing, or late-stage mergers (e.g., Davis et al. 2011; Barrera-Ballesteros et al. 2015; Jin et al. 2016).

3.3.4. The Receding Shell C1

On the eastern side of the AGN nucleus, a red wing is present in each of the strong emission lines, which is highlighted in Figure 6. From north to south, the fitted radial velocities and velocity dispersions are constant across the characteristic with mean values of $v_{\mathrm{red,C1}} = 40 \pm 2\ \mathrm{km\ s^{-1}}$ (Hβ, [O III]) and $\sigma_{\mathrm{red,C1}} = 132 \pm 2\ \mathrm{km\ s^{-1}}$ (Hα, [N II], [S II]) respectively (see Appendix A for the spectral fit). We highlight the spots with maximum luminosities at fixed decl. in Figure 6. The resulting structure appears to be shell shaped.

3.3.5. Morphology of the Underlying Structure

C1 is likely affected by beam smearing since its emission line kinematics are almost constant across the structure. However, the spatial profile of C1 does not appear to be PSF-like, which could suggest that the observed emission is the result of the PSF convolved with some other underlying emission. Thus, our objective is to obtain spatial information on the possible underlying structure. The detailed procedure of how we extract the underlying structure is described in Appendix B. We find that the intrinsic morphology of the gas cloud is similar to a shell, with a distance of 308 mas (250 pc) from the nucleus.

3.3.6. The Clumpy Gas in the UV

The NUV image taken with HST/WFC3 exhibits structures in HE 0040-1105's host galaxy, which we detect at the $>3\sigma$ and $>5\sigma$ confidence levels, respectively. They are located on the outskirts of the PSF, ∼800 mas or 660 pc northeast of the AGN location. In Figure 6, we highlight the structures together with the deconvolved profile of the shell-like C1 feature, whose locations appear to coincide. Possible explanations include

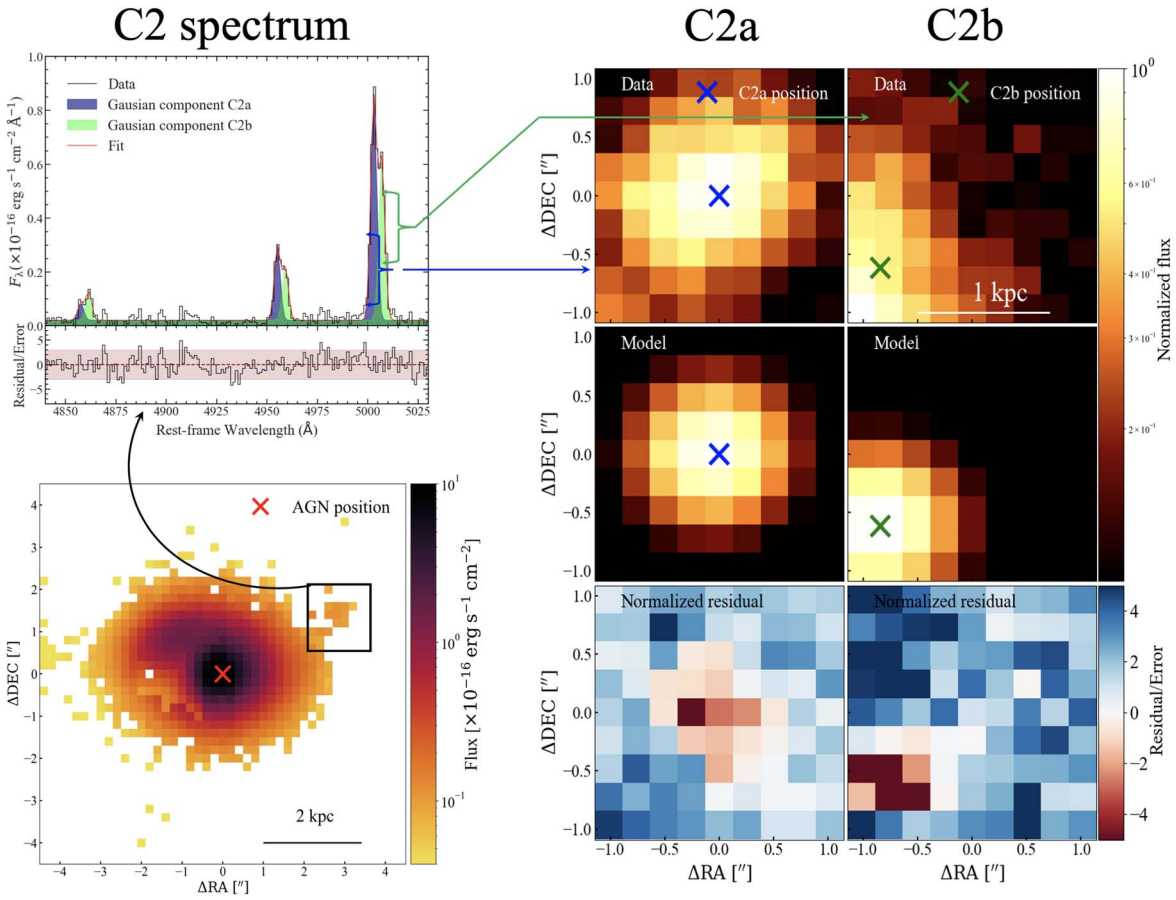

Figure 7. Spectroastrometric analysis of the multicomponent [O III] cloud C2. Lower left panel: 2D flux profile of [O III] with C2 being highlighted with a box (upper panel). Upper left panel: optical Hβ + [O III] spectrum extracted from a 9 × 9 spaxel aperture, and its multicomponent fit. The gray lines describe the data, and the blue and green-shaded Gaussian components correspond to the regions C2a and C2b, respectively (top panel). The residual spectrum is divided by the error spectrum. The brown-shaded region defines the residuals within 3σ and the red dotted line indicates a region with zero residual (bottom panel). Right panel: 2D Moffat modeling results for C2. From top to bottom, the panels show the measured Σ_{2D}, the corresponding best-fit 2D Moffat model, and the residual maps normalized by the uncertainty. From left to right, the panels correspond to C2a and C2b. The blue and green crosses indicate the flux-weighted centroids of C2a and C2b. The Σ_{2D} profile of C2a is well described by the Moffat PSF, whereas, for C2b, the Moffat model leads to high residuals.

clumpy outflows (Takeuchi et al. 2013), accretion of gas onto the nucleus (Tremblay et al. 2016), and gas clumps due to a merger (Arata et al. 2018). We notice that $\sigma_{\rm red,C1}$ agrees with σ_* within uncertainties, implying that these gas clouds could undergo a virial motion influenced by the bulge potential (Nelson & Whittle 1996) and hence may not be a part of the nuclear outflow. However, this clumpy gas detected in the NUV is also consistent with HE 0040-1105 being a late-stage merger, which is in line with our findings in Section 3.3.2. Therefore, the host galaxy of HE 0040-1105 is most likely a merger-remnant.

3.3.7. Multicomponent Cloud C2

The ionized gas clouds emitting in [O III] have a radial velocity of $v_{\rm [O\,III]} \sim -200\,{\rm km\,s^{-1}}$ and dispersion of $\sigma_{\rm [O\,III]} \sim 70\,{\rm km\,s^{-1}}$ (Figure 4(c)). To determine the associated gas kinematics, we inspect the emission line spectrum Hβ + [O III] by co-adding spectra from a 9 × 9 spaxel aperture, enabling us to achieve an S/N > 5 in the emission lines. The bright [O III] emission line allows one to disentangle two components. Hα + [N II] + [S II] emission lines have an S/N < 3 in each spaxel in C2. In order to infer the ionization condition we co-add spectra from the similar 9 × 9 and achieve an S/N > 4, which we fit with a multi-Gaussian model and notice similar double-peaked emission lines (see Appendix A). However, we constrain our analysis to Hβ + [O III] emission lines due to the availability of higher S/N spectra. The Hβ + [O III] spectrum contains a double-peaked emission line profile, which we model with a superposition of kinematically coupled Gaussian components. The AIC criterion suggests that two Gaussian components C2a and C2b for each of the corresponding emission lines are sufficient to describe the shape of the emission line of C2. C2a is blueshifted by $v_{\rm [O\,III]}$, C2a $\sim -220\,{\rm km\,s^{-1}}$, while C2b is redshifted by $v_{\rm [O\,III]}$, C2b $\sim +30\,{\rm km\,s^{-1}}$.

3.3.8. Origin of the C2 Gas Clouds

We perform a spectroastrometric analysis within 9 × 9 pixels (1.″8 × 1.″8) to spatially locate C2a and C2b according to Singha et al. (2022). The FWHM of the MUSE PSF >3 pixels makes any result derived from the analysis within the 3 × 3 pixel diameter region unreliable. Choosing a larger aperture produces a much more robust fit. We find that C2a is spatially unresolved by MUSE, whereas C2b appears to be spatially resolved. The projected offset between the flux-weighted centroids of C2b and C2a is 682 ± 28 pc. As seen in Figure 7, the spatial morphology of C2b suggests that it is part of the ionized gas emission from the EELR. The projected offset between the flux-weighted centroid of C2a and the AGN

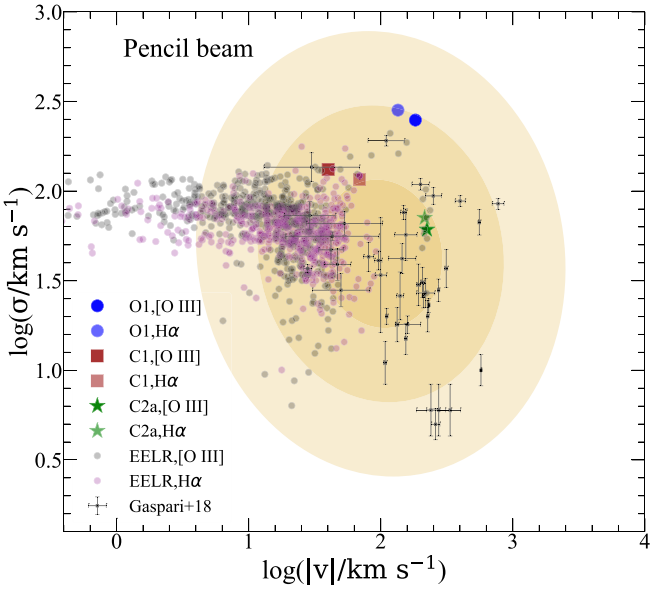

Figure 8. Kinematical diagnostic (k-plot) comparing the line broadening vs. line shift, with a pencil-beam approach (pixel-by-pixel). The yellow contours show the 1σ–3σ confidence intervals predicted by CCA simulations, while the black points denote a diverse sample of central and isolated galaxies (see Gaspari et al. 2018). We overlay the results for the [O III] emitting ionized gas in the O1 outflow (blue circles), C1 shell (brown square), and isolated [O III] cloud C2a (green stars). We adopt similar but light-colored markers to denote the Hα-emitting gas clouds. The small gray and purple circles denote the ionized [O III] and Hα gas in the EELR. Most gas elements are within the $\sim 2\sigma$ CCA contours suggesting that our main features are likely experiencing turbulent multi-phase condensation, which will soon stimulate a rain back on the SMBH.

nucleus of HE 0040-1105 is ~2.6 kpc. Its isolated morphology and sub-virial kinematics (velocity dispersion $<\sigma_*$) suggest that the gas in C2a is unlikely to be a part of the nuclear AGN-driven outflow.

3.3.9. Hα-emitting Cloud C3

Another component C3 is located at a large distance from the nucleus ($d \sim 3$ kpc). As opposed to C2, this feature is only present in Hα + [N II] + [S II], but not in Hβ + [O III]. The ionized gas cloud is slightly redshifted with respect to the EELR thin disk rotation with $\sigma_{\rm H\alpha} = 40 \pm 2$ km s^{-1}. However, in Figure 2(c), a thin disk model well predicts the receding line-of-sight velocity on the location of C3, which is further confirmed by the velocity residuals' scatter around the rest-frame velocity (Figure 2(f)). Our results suggest that the thin-rotating disk model describes the velocity structure of C3. Since the ionized gas clouds in C3 seem to follow the regular rotation pattern of the EELR, we conclude that C3 is a structure that is embedded in the EELR. The compactness of C3 may therefore be explained by the sensitivity limit of the observation, rather than C3 being an independent gas cloud.

3.3.10. Chaotic Cold Accretion and Condensation

While the motions of the gas are globally affected by the bulge potential in situ, the cloud elements will be also affected by other relevant physical processes. In particular, whenever there are some significant perturbations driven in the gaseous atmospheres, the gas will rapidly condense via turbulent thermal instability (e.g., Gaspari et al. 2013). In HE 0040-1105, AGN feedback will create fluctuations at small radii. At large scales, the merger environment will further augment the density fluctuations (e.g., Lau et al. 2017) in the ISM, which will quicken the multi-phase precipitation. To test this, we use the kinematic diagnostic ("k-plot"; Gaspari et al. 2018) which confronts the line-of-sight velocity v against the line-of-sight velocity dispersion σ (Table 3), in logarithmic space. This is an insightful diagnostic leveraged in several recent studies (see also Maccagni et al. 2021; North et al. 2021; Temi et al. 2022).

We show the k-plot in Figure 8, superposed to the confidence intervals predicted by high-resolution CCA simulations. Such a diagnostic is very useful here to dissect different physical mechanisms acting on the cold/warm gas. Gas clouds located in the top left quadrant often undergo macroturbulent motions in the galactic/group halo. In contrast, ionized gas with both high velocity and dispersion (top right quadrant) are more likely affected by the outflow kinematics. Cloud elements that reside in the bottom right quadrant are often associated with fast microscale inflows falling onto the SMBH. Cloudlets residing in the central 1σ–2σ contour regions are likely experiencing CCA condensation rain, eventually falling back onto the nuclear region.

As shown in Figure 8, our HE 0040-1105 C1 (red) and C2a (green) points reside within the central 2σ CCA (yellow) contour, regardless of the line used. Thus, alongside their moderate velocities, this suggests that C1 and C2a elements are likely prone to multi-phase condensation, and will soon rain back onto the AGN (mainly via the cloud inelastic collisions). The O1 components are instead more elevated, closer to the upper regions, thus suggesting that such gas is still significantly tied to the outflow thrust, yet capable of moderate condensation. Considering the extended complex of ionized gas, the bulk of the Hα (gray) and [O III] (purple) points still fall within the CCA region, albeit we notice a left straight tail of gas affected by rotation. Overall, on top of pure gravitational dynamics, CCA and related turbulent condensation are likely important physical components acting in HE 0040-1105.

3.4. Morphology of the Radio Emission

3.4.1. Subkiloparsec Scales Traced by VLA

Our main objective in this section is to compare the O1 outflow to the observed radio emission spatially. We show the radio continuum images of HE 0040-1105 at 6 and 10 GHz obtained using VLA in Figure 9. In order to extract the intensity and morphology of the bright spot in the center, we run the `imfit` task included in CASA on the VLA *C*- and *X*-band radio images. For the measured flux densities, we follow the conservative approach from Panessa et al. (2022) and consider the total uncertainty σ_{S_ν} of the peak brightness, which involves both the systematic uncertainty from the `imfit` task, and the statistical uncertainty, which equals the sum in quadrature of the off-source rms of the image $\sigma_{\rm off}$ plus the 5% calibration uncertainty ϵ times the peak brightness S_ν.

We derive the total uncertainty from the quadrature sum of the individual contributions $\sigma_{S_\nu} = (\sigma_{\rm off}^2 + (\epsilon S_\nu)^2)^{1/2}$. The results obtained from our `imfit` analysis are tabulated in Table 4. We notice that the major and minor axes of the deconvolved structure in both images (Figure 9) agree within their uncertainties. The similar spatial extensions of the underlying radio emission deconvolved from the clean beam in both 6 and 10 GHz observations confirm the detection of extended radio emission on <500 pc scales. Comparing

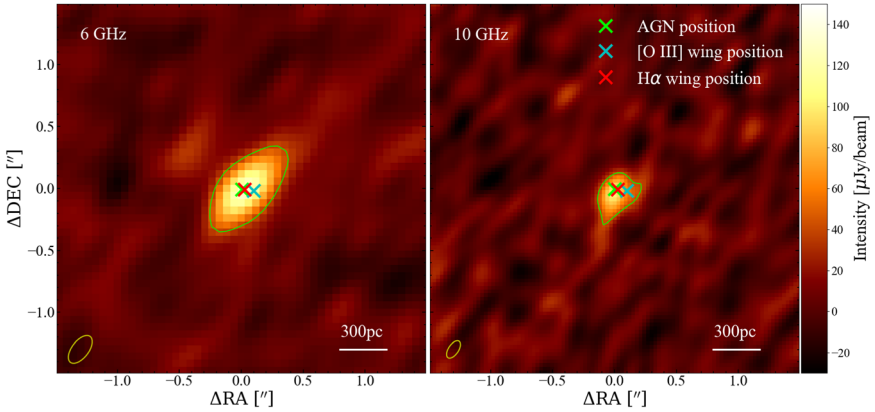

Figure 9. VLA continuum images of HE 0040-1105 in the central 3″. Left panel: the 6 GHz image with the yellow contour in the bottom left indicates the clean beam ($0\overset{''}{.}53 \times 0\overset{''}{.}27$ and PA $= -36\overset{\circ}{.}9$). Right panel: the 10 GHz image with yellow contour indicating the clean beam ($0\overset{''}{.}26 \times 0\overset{''}{.}17$ and PA $= -22°$). Green contours correspond to the 5σ sensitivity levels at 35 and 40 μJy for the *C*- and *X*-bands, respectively. The spectroastrometric positions of the AGN, [O III] wing, and Hα components are highlighted as green, red, and cyan crosses, respectively.

Table 4
Orientation and Morphology of the Identified Radio-emitting Regions

Facility	Frequency (GHz)	Region	Morphology	FWHM (mas)	PA (deg)	Peak Brightness (μJy beam^{-1})	Integrated Flux Density (μJy)
RACS	0.88	⋯	⋯	<25,000 × 25,000	⋯	1740 ± 340	3740 ± 690
EVN	1.67	S0	Unresolved	<20 × 10	⋯	83.7±10.4	82 ± 12
EVN	1.67	S1	Unresolved	<20 × 10	⋯	48.1 ± 7.8	34.0 ± 8.0
EVN	1.67	S2	Unresolved	<20 × 10	⋯	44.4 ± 7.6	43.0 ± 9.6
EVN	1.67	S3	Unresolved	<20 × 10	⋯	57.8 ± 8.4	41 ± 12
VLASS	3	⋯	⋯	<2500 × 2500	⋯	678 ± 140	1370 ± 500
VLA	6	O1	Resolved	(392 ± 133)×(226 ± 85)	132 ± 74	125 ± 10	204 ± 26
VLA	10	O1	Resolved	(238 ± 85)×(163 ± 94)	109 ± 52	92 ± 11	171 ± 28

Note. From left to right, the columns denote the facility used, the central frequency in the observed frequency band, different regions in the radio emission, spatial morphology denoting if the emission is compact (unresolved) or extended (resolved), the major and minor axes of the deconvolved source from the clean beam, PA of the deconvolved source, the peak brightness, and the integrated flux density. In the case of unresolved radio emission, we tabulate the clean beam size as the upper limits of the underlying radio emission convolved with the clean beam. Archival radio interferometric observations from RACS and VLASS are listed as well.

observations from two different instruments requires a point of reference, for which we chose the AGN location. We assume that the AGN is located at the centroid of the brightest spots in the center of the VLA images or the radio core. We identify the Hβ BLR centroid with the radio core in the VLA image. In Figure 9, we notice that the flux-weighted centroids of [O III] and Hα in O1 overlap with the radio VLA *C*- (6 GHz) and *X*- (10 GHz) band continuum emission. Such spatial coincidence suggests that the radio emission detected in VLA is either produced due to the outflows, or the outflows produce the radio emission. However, one more possibility is that the radio structures happen to be co-spatial with the centroids of the outflow without any connection between them.

From our VLA observations, we estimate values of the spectral indices from the peak brightness and the integrated flux density as $\alpha_{\rm peak} = -0.60 \pm 0.28$ and $\alpha_{\rm int} = -0.34 \pm 0.41$, respectively. The uncertainties associated with the spectral indices are evaluated as per Panessa et al. (2022). As the peak brightness is not subjected to the different beam sizes in different frequencies, we use $\alpha_{\rm peak}$ throughout the paper.

3.4.2. Previous Radio Observations

The radio source in HE 0040-1105 is undetected in the FIRST survey (Becker et al. 1995), giving an upper limit to the integrated flux density of 1 mJy at 1.4 GHz. The source is detected in the VLASS survey (Lacy et al. 2020) at 3 GHz. The peak brightness and the integrated flux density are 0.678 mJy beam^{-1} and 0.810 mJy, respectively. The measured 3–6 GHz spectral index ($\alpha_{3-6\,\rm GHz}$) is steep with $\alpha_{3-6\,\rm GHz} = -2.4$. The Rapid ASKAP Continuum Survey (RACS) has also detected the radio source at 880 MHz with a resolution of $25'' \times 25''$. The peak brightness and flux density values for this detection are tabulated in Table 4.

3.4.3. Parsec Scales Resolved by EVN

Despite the VLA's high spatial resolution, it cannot resolve the central 200 pc aperture region where the flux-weighted centroids of the outflowing gas are located. The very high-resolution imaging capability of EVN at 18 cm resolves <10 pc scales. Figure 10 shows one-sided parsec-scale radio emission obtained using the EVN. We detect four compact radio knots (S0, S1, S2, and S3) over 3σ confidence, and in the brightest knot S0 we measure an S/N ~ 6.

We assume that the flux-weighted centroid of S0 is the radio core and align it with the astrometric BLR Hβ center. The angular resolution of EVN is two orders of magnitude higher than MUSE WFM. To account for this difference, we use 3σ uncertainties of the astrometric locations of the flux-weighted Hα and [O III] centroids. In Figure 10, we show that S1 overlaps with the flux-weighted Hα centroid, while S3 is in the

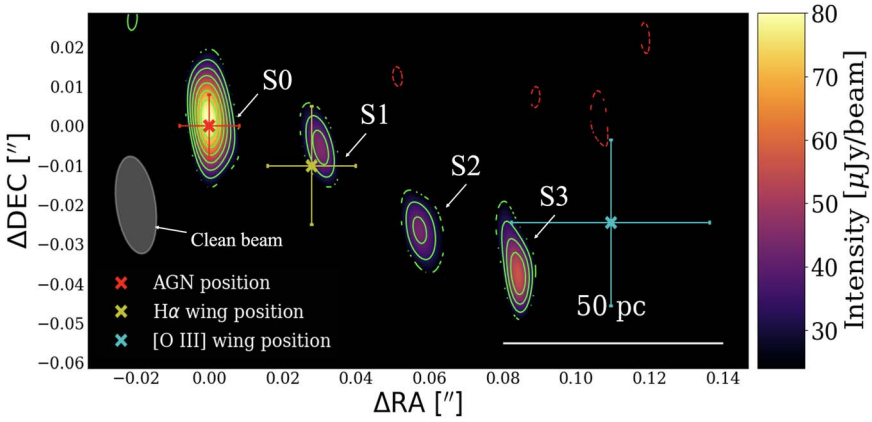

Figure 10. EVN contour image of HE 0040-1105 at 18 cm. The image shows four unresolved components. We identify the brightest component S0 with the galaxy nucleus and name the remaining components S1, S2, and S3. The synthesized beam is 24.9 × 10.7 mas at an 8.°97 PA and is shown on the left edge of the image as a gray-shaded ellipse. The contour levels are −30%, 30%, 40%, 50%, 60%, 70%, 80%, and 90% of the peak intensity 83.7 μJy beam^{-1}. The positive contours are plotted with green lines, whereas the negative contours are indicated with red lines. The crosses describe the flux-weighted centroids of the AGN (red), the Hα blue wing (yellow), and the [O III] blue wing (cyan) emission. The associated error bars indicate the 3σ uncertainties of the respective locations determined using spectro-astrometry. Assuming the brightest spot in S0 originates from the AGN, S1 and S3 overlap with the flux-weighted centroids of the blue wings within their uncertainties.

vicinity of the flux-weighted [O III] centroid. The radio knots are all directed toward the southwest, and thus appear to be aligned along one axis. The morphological parameters of the regions were estimated by fitting their flux profiles with a 2D Gaussian using the AIPS task JMFIT. They are summarized with their uncertainties in Table 4.

3.4.4. Radio Spectrum of the Source

The 880 MHz–10 GHz radio spectrum of HE 0040-1105 (Figure 11) is consistent with a straight spectrum, and a power-law fit yields a spectral index, $\alpha_{\rm int,0.88-10\ GHz} = -1.30 \pm 0.28$. There is no evidence for either a peak or break in the spectrum over the observed frequency range. The integrated flux density ($S_{\rm int}$) in the EVN observations is much lower than the expected $S_{\rm int}$ assuming a power-law extrapolation from the lower-resolution data. Such a discrepancy in $S_{\rm int}$ suggests that the EVN is resolving out a larger-scale structure.

As mentioned earlier, the upper limit to its flux density at 1.4 GHz is $S_{\rm Thr,FIRST} \sim 1$ mJy. However, the radio spectrum shown in Figure 11 suggests an extrapolated flux density of 1.52 ± 0.26 mJy. This discrepancy is possibly due to variability of the radio source since the FIRST observations were taken in 1995 and the VLA observations at 3, 6, and 10 GHz were taken in the last few years. Similar radio variability is seen in other radio-quiet AGN (e.g., Falcke et al. 2001; Nagar et al. 2002; Barvainis et al. 2005; Mundell et al. 2009).

4. Discussion

Combining the optical VLT/MUSE with HST images has revealed multiple kinematic components in HE 0040-1105's ionized gas emission. Together with the radio interferometric observations from VLA and EVN, we were able to resolve compact radio-emitting regions that are close to the galaxy nucleus from where an ionized gas outflow is launched. In this section, we combine spatial information from optical and radio observations to (i) discuss the origin of radio emission in Section 4.1.2, (ii) investigate the outflow launching mechanism in Section 4.2, and (iii) explore whether the ionized gas outflow can escape the host galaxy in Section 4.3.

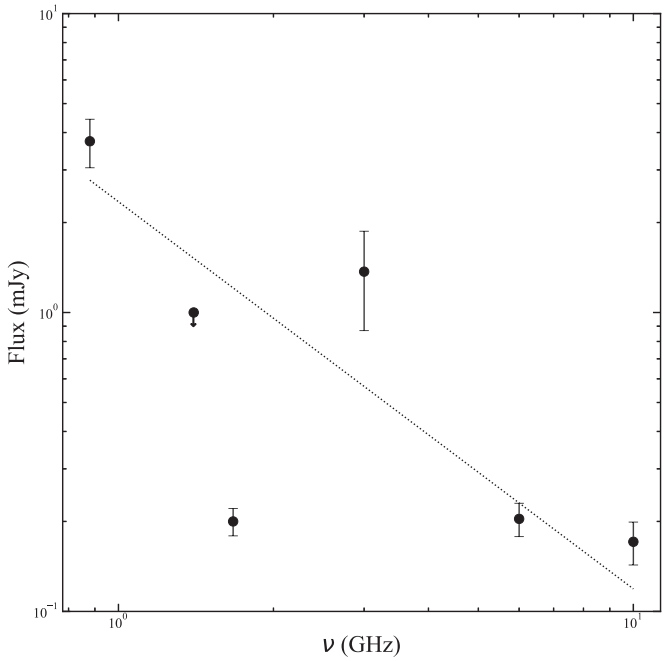

Figure 11. Radio continuum spectrum for HE 0040-1105 between 880 MHz and 10 GHz, showing the variation of the integrated flux density values (millijansky) with frequency. Note that we include only the upper limit for the VLA FIRST survey. The black dashed line indicates the best-fitted power-law model to the radio spectrum within the frequency range 880 MHz–10 GHz, yielding a spectral index of $\alpha_{\rm int,0.88-10\ GHz} = -1.30 \pm 0.28$. We ignored the EVN observation during the fitting procedure as it could capture only a small fraction of the source's flux density. The radio spectrum is most consistent with a steep spectrum component.

4.1. Origin of the Radio Emission

4.1.1. AGN Coronal Emission

If S0 is the AGN's radio core, then the AGN corona's synchrotron emission will contribute to the observed radio emission from S0. Laor & Behar (2008) studied 71 radio-quiet and 16 radio-loud Palomar–Green AGN (Green et al. 1986). Radio luminosities ($L_{\rm R}$) and X-ray luminosities ($L_{\rm X}$) in the radio-quiet AGN follow $L_{\rm R}/L_{\rm X} \sim 10^{-5}$ (Güdel & Benz 1993),

which is usually seen in coronally active stars. The X-ray component is caused by thermal free–free emission from the hot $T \sim 10^7$ K plasma, whereas the radio component is caused by nonthermal synchrotron emission. However, the coronal radio emission is produced on scales of a few hundred SMBH Schwarzschild radii (Panessa et al. 2019; Wilkins et al. 2021). The projected offset between S0 and the closest knot S1 is ∼15 pc, which is a few orders of magnitude higher than where the radio emission from the corona would be produced. Therefore S1, S2, and S3 are not produced due to the coronal emission.

4.1.2. Star-forming Processes

To estimate whether HE 0040-1105's radio emission can be explained by processes that are related to star formation, we estimate the nuclear SFR and compare it with the value derived from the Hα luminosity (Section 3.2.4). Assuming that the entire radio emission originates from star formation-related processes, we utilize the VLA *X*-band observations to infer the central 1″ SFR from where the emission originates. The integrated flux density at 10 GHz is $S_{10\ \mathrm{GHz}} \sim 171\ \mu$Jy. Using the spectral index derived from the peak brightness, $\alpha \sim -0.6$, the integrated flux density at 1.4 GHz becomes $S_{1.4\ \mathrm{GHz}} \sim 556\ \mu$Jy. The 1.4 GHz SFR ($\mathrm{SFR}_{1.4\ \mathrm{GHz}}$) can be estimated following the calibration prescribed by Murphy et al. (2011):

$$\frac{\mathrm{SFR}_{1.4\ \mathrm{GHz}}}{M_\odot\ \mathrm{yr}^{-1}} = 6.35 \times 10^{-29}\left(\frac{L_{1.4\ \mathrm{GHz}}}{\mathrm{erg\ s^{-1}\ Hz^{-1}}}\right), \quad (7)$$

where $L_{1.4\ \mathrm{GHz}}$ is the radio luminosity at 1.4 GHz.

We estimate $\mathrm{SFR}_{1.4\ \mathrm{GHz}} = 1.45\ M_\odot\ \mathrm{yr}^{-1}$, which is more than two orders of magnitude higher than the $\mathrm{SFR}_{\mathrm{O1}}$ derived in Section 3.2.4. This suggests that supernovae and star-forming processes alone cannot explain the observed radio emission in the central 1″ aperture. Therefore, at least one other process is required to explain HE 0040-1105's radio luminosity in the central 1″ aperture region. The existence of supernovae clusters in the nuclear (<100 pc) region cannot be easily ruled out.

The total 1.4 GHz radio luminosity of the knots S0, S1, S2, and S3 is 1.09×10^{21} W Hz^{-1}. If we assume that the observed radio luminosity measured in these knots originates entirely from star formation-related processes, the predicted SFR of $0.69\ M_\odot\ \mathrm{yr}^{-1}$ is still two orders of magnitude higher than $\mathrm{SFR}_{\mathrm{O1}}$. We conclude that S0-S3 are therefore not clusters of supernovae. The spatial alignment of the radio knots suggests that they are parts of a collimated radio-emitting structure.

4.1.3. AGN Wind versus Jet

Zakamska & Greene (2014) proposed that the shocks from AGN-driven winds could give rise to nonthermal radio emissions. They suggested that the AGN wind could escape through the path of least resistance, and the radio emission produced by these winds would be diffuse. A recent study by Liu et al. (2022) using the Very Large Baseline Array has suggested that radio emission produced by AGN winds may not contain any compact structures. On the other hand, we detect compact radio knots on parsec scales in our EVN observations. If the findings of Liu et al. (2022) are true, the parsec-scale knots detected in our EVN observations are likely to be a jet. However, these radio structures lack a traditional linear jet-like morphology as can be seen (e.g., Huchra & Burg 1992; Brunthaler et al. 2000; Thean et al. 2001). Another possibility is that the jets and the winds could operate at the same time. Agudo et al. (2015) suggested that if the mass loading of the disk-driven wind cannot produce an ultra-relativistic flow, both jets and winds could operate simultaneously.

4.2. Driver of the Outflow

4.2.1. Constraints from the Outflow Energetics

The radio properties of the observed emission cannot explain its connection to the outflow. A one-to-one connection could only be established if the momentum and kinetic energy injection by the wind or jet is greater than those of the outflowing ionized gas. The momentum injection due to AGN radiation can be calculated as $\dot{P}_{\mathrm{AGN}} \sim L_{\mathrm{bol}}/c \sim 4.6 \times 10^{33}$ dyne. In Figure 5, $\dot{P}_{\mathrm{ion,cone}}/\dot{P}_{\mathrm{AGN}} < 1$ for all values of v_{out}, while $\dot{P}_{\mathrm{ion,shell}} < \dot{P}_{\mathrm{AGN}}$ only for $v_{\mathrm{out}} = v_{\mathrm{broad}}$ when $\Delta R > 180$ pc. This momentum boost indicates that the outflow is likely to be energy conserving (Faucher-Giguère & Quataert 2012). L_{bol} can easily produce the observed injection rate of kinetic energy from the outflow. We find that ∼20% of the optical bolometric luminosity of the AGN can produce the maximum predicted kinetic energy injection rate $\dot{E}_{\mathrm{ion,max}} \sim 3 \times 10^{43}$ erg s^{-1}. Therefore, the AGN radiation pressure can drive these outflows.

However, the existence of the compact knot-like feature in our EVN observation is more likely to be produced by a jet. Assuming that the entire observed VLA radio emission is due to a jet, the estimated 1.4 GHz radio luminosity is $\log(L_{1.4\ \mathrm{GHz}}/\mathrm{W\ Hz^{-1}}) \sim 21.37$. Using the scaling relations of radio power versus jet power given by Cavagnolo et al. (2010), we estimate that the associated jet power (P_{jet}) is $\sim 1.3 \times 10^{42}$ erg s^{-1}, with an upper limit of 5.8×10^{42} erg s^{-1}. P_{jet} is about an order of magnitude higher than $\dot{E}_{\mathrm{ion,\ cone}}$ and $\dot{E}_{\mathrm{ion,shell}}$ except when $v_{\mathrm{out}} = v_{\mathrm{max}}$.

4.2.2. Constraints from the Ionization Mechanism

We estimate $\log([\mathrm{O\ III}]/\mathrm{H}\beta) = 0.81 \pm 0.04$ and $\log([\mathrm{N\ II}]/\mathrm{H}\alpha) = -1.09 \pm 0.07$, which places O1 between the composite and AGN-photoionized regions in the BPT diagram (Baldwin et al. 1981, see Figure 12). As we have discussed in Section 4.1.1, the energy and momentum contribution from star-forming-related processes is not sufficient to power the ionized gas outflow. To test whether the AGN radiation can power the O1 outflow we estimate the ionization parameter U, which represents the ratio of ionizing photon flux to the electron density of the ambient medium, and is defined as

$$U = \frac{Q}{4\pi r^2 n_{\mathrm{H}} c}, \quad (8)$$

where, $L_{\mathrm{ion,O1}}$ is the luminosity of the ionizing source, ν is the frequency of the ionizing radiation, h the Planck constant, r the distance from the ionizing source, and $n_{\mathrm{H}} \sim 0.85 n_{\mathrm{e}}$ the hydrogen number density per unit area (Crenshaw et al. 2015). The ionization parameter U can be estimated from the

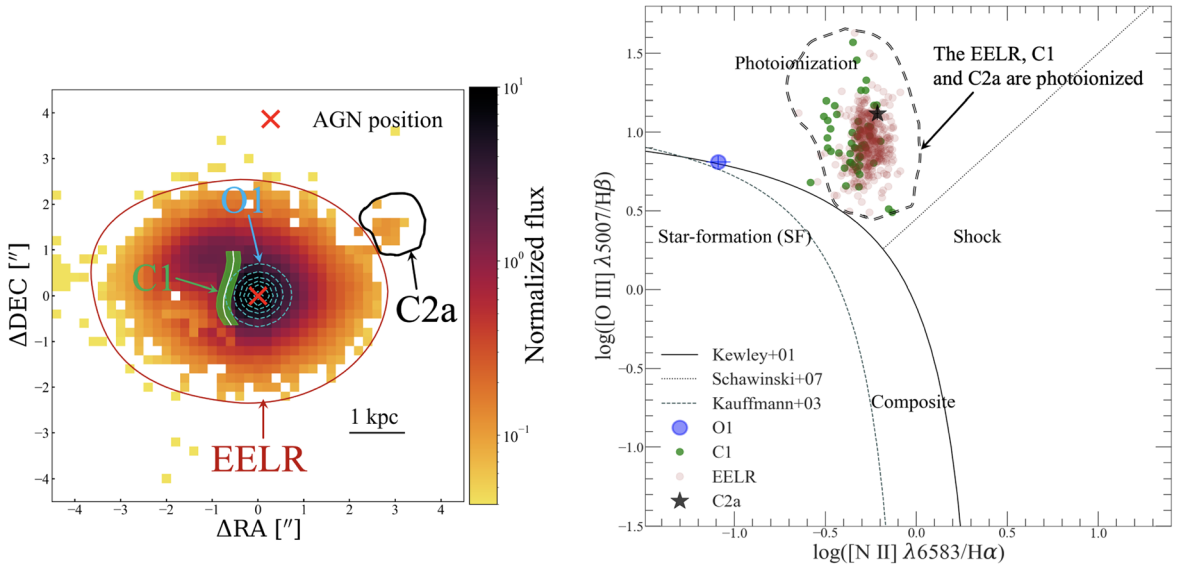

Figure 12. BPT diagram showing the [O III] $\lambda5007/\mathrm{H}\beta$ vs. [N II] $\lambda6583/\mathrm{H}\alpha$ ratios for different regions across the entire ionized nebula. Left panel: [O III] flux map with the extraction of different regions shown by curved lines and arrows. The red cross denotes the AGN location. Right panel: the black dotted line represents the upper limit of ionization due to pure star formation. The region between the black dotted line and the black solid line represents ionization due to both star formation and AGN. The area within the black and gray solid lines represents ionization due to shock. Above the black and gray solid lines, the hard ionization photoionizing field from the AGN dominates the line ratios. The blue cross and black stars describe the regions O1 and C2a, respectively, and are plotted with error bars with similar colors. The green and brown dots represent the feature C1 and the EELR and are not plotted with error bars because they are spatially resolved. O1 resides between the composite and AGN-photoionized region within uncertainties. The EELR, C1, and C2a are photoionized by the AGN.

emission line ratios (Baron & Netzer 2019)

$$\log U = +0.191\left[\log\left(\frac{[\mathrm{O\ III}]}{\mathrm{H}\beta}\right)\right] + 0.778\left[\log\left(\frac{[\mathrm{O\ III}]}{\mathrm{H}\beta}\right)\right]^2 - 0.251\left[\log\left(\frac{[\mathrm{N\ II}]}{\mathrm{H}\alpha}\right)\right] + 0.342\left[\log\left(\frac{[\mathrm{N\ II}]}{\mathrm{H}\alpha}\right)\right]^2 + 3.766.$$

For the ionized gas outflow O1, we estimate U and the associated uncertainty with a Monte Carlo approach, yielding $\log U = -2.42 \pm 0.08$.

As we use the 5100 Å continuum luminosity to estimate the optical bolometric luminosity of the AGN, the corresponding frequency at that wavelength is $\nu = c/(5100\,\mathring{A}) = 5.77 \times 10^{14}$Hz. Using $Q = L_{\mathrm{ion}}/h\nu$, we estimate the ionizing luminosity as $L_{\mathrm{ion,O1}} = (1.05\text{–}1.1) \times 10^{43}\mathrm{erg\,s^{-1}}$. This value is an order of magnitude lower than L_{bol}, indicating that the bolometric luminosity of the AGN may not be able to photoionize the gas clouds, i.e., is not able to produce the emission line ratios observed in O1.

A scenario in which the AGN radiation may still be the powering mechanism is provided by optically thick gas clouds blocking a significant fraction of AGN radiation. This may lead to an AGN luminosity that is higher than the estimated value from the emission line ratios $L_{\mathrm{ion,O1}}$. We estimate the column density in O1 ($N_{\mathrm{H,O1}}$) using the N_{H}–A_{V} scaling relation from Güver & Özel (2009), as follows:

$$N_{\mathrm{H,O1}} = (2.21 \pm 0.09) \times 10^{21} A_{\mathrm{V,O1}}\,\mathrm{cm^{-2}}, \quad (9)$$

yielding $N_{\mathrm{H,O1}} = (6.0 \pm 1.5) \times 10^{21}\mathrm{cm^{-2}}$, i.e., an optically thin outflow O1. The clouds only become optically thick when they reach a hydrogen column density value $>10^{23}\,\mathrm{cm^{-2}}$ (Jaffarian & Gaskell 2020). Therefore, the optically thin clouds may not be able to block >90% of the incoming ionizing luminosity from the AGN and produce the observed low value of $L_{\mathrm{ion,O1}}$. We note, however, that there have been other mechanisms proposed that could shield radiation from the AGN, but not be reflected in our estimate for N_{H}. They include self-shielding from ionized gas (Zubovas & Bourne 2017) and screening due to the shadow of the host disk (Husemann et al. 2019).

4.2.3. O1 Outflow Powering Mechanism

We now explore the possibility of weak radio jets being the ionizing source of the O1 outflow. Although the upper limit of P_{jet} is a factor of 2 lower than $L_{\mathrm{ion,O1}}$ at $r = 480$ pc (Section 4.1.3), P_{jet} agrees well with the possible attainable values for $L_{\mathrm{ion,O1}}$ estimated at the location of the ionized gas outflow at $r = 150$ pc, which is in the vicinity of the radio source S1. In Singha et al. (2022), we found that (99 ± 1)% of the observed outflowing [O III] emission is located at the flux-weighted centroid. For an AGN wind-driven outflow, as the wind propagates along every possible direction, the bulk of the [O III] emission is unexpected to be located at one particular region. Together with the close proximity of the entirety of the ionized gas outflow emission to the collimated radio jet-like structure, where the comparability of the ionizing luminosity of the outflowing gas is comparable to the jet power, we propose that weak radio jets could drive this ionized outflow at its location. However, AGN radiation is necessary to carry the gas to larger distances, which is necessary to explain the high ionizing luminosity $L_{\mathrm{ion,O1}}$ on 500 pc scales.

We propose that the radio jets could transfer their mechanical energy to the ambient gas, and therefore perturb and ionize the clouds in their vicinity. As they move outward with the photons from the ionization cone, they gradually become photoionized, which is in line with the two-stage acceleration mechanism proposed by Hopkins & Elvis (2010). Our analysis of the ionized gas outflow is limited by both sensitivity and finite spatial resolution, which also limits our

understanding of the complex interaction between radio emission, AGN radiation field, and the host galaxy ISM in HE 0040-1105.

Smirnova-Pinchukova et al. (2022) found that the large ionized gas nebula EELR is largely photoionized. However, their analysis did not involve the resolved analysis of the ionized gas outflow O1 and the clouds C1 and C2a. In the BPT diagram shown in Figure 12, it becomes evident that each of the clouds C1 and C2a is photoionized.

4.3. Outflow Escaping the Host Galaxy Gravitational Potential

While numerous studies have shown that AGN-driven outflows are able to deprive galaxies of their gas component (e.g., Benson et al. 2003; Bower et al. 2006; Moll et al. 2007; Schindler & Diaferio 2008; McCarthy et al. 2010; Gaspari et al. 2011; Crenshaw & Kraemer 2012; McNamara & Nulsen 2012; Schaye et al. 2015; Gaspari et al. 2018), there is a significant fraction of the outflowing material that falls back and may eventually be accreted by the AGN (Oppenheimer et al. 2010; Diniz et al. 2015; Gaspari et al. 2013; Muratov et al. 2015; Gaspari & Sądowski 2017; Wittor & Gaspari 2020). To test whether HE 0040-1105's outflowing ionized gas can escape the host galaxy's gravitational potential, we assume an inclination of $i = 40°$ and estimate its escape velocity ($v_{\rm esc,ion}$) of the ionized gas from the host, and assume an inclination of $i = 40°$ throughout the entire analysis. We follow the prescription of Rupke et al. (2002), which uses the gravitational model of an isothermal sphere to estimate $v_{\rm esc,ion}$ at a distance r from the AGN nucleus as

$$v_{\rm esc,ion}(r, r_{\rm max}) = \sqrt{2}\, v_{\rm rot}[1 + \ln(r_{\rm max}/r)]^{1/2}\,, \qquad (10)$$

where $v_{\rm rot}$ is the rotational velocity of the host galaxy. Following Villar-Martín et al. (2017), we estimate $v_{\rm rot} = \sqrt{2}\,\sigma_* \sim 181$ km s^{-1}.

In the above, r represents the distance from the AGN nucleus and $r_{\rm max}$ is the maximum radius of the dark matter halo, which is observationally unconstrained. We estimate $r_{\rm max}$ from the scaling relation (Huang et al. 2017) between the virial radius of the dark matter halo and the deprojected host galaxy effective radius $R_{\rm eff} = 9.6$ kpc (Husemann et al. 2022) as $r_{\rm max} \sim 420$ kpc. Our estimate for $r_{\rm max}$ should be regarded as an upper limit since studies of outflows in quasar host galaxies often assume $r_{\rm max} = 100$ kpc (e.g., Greene et al. 2011; Villar-Martín et al. 2017; Herrera-Camus et al. 2019). For the escape velocity at the outer boundary of O1, where $r = 480$ pc and $r_{\rm max} = 420$ kpc we estimate $v_{\rm esc} \sim 710$ km s^{-1}, which is higher than the maximum velocity of the outflow $v_{\rm max}$ (see Table 3). For $r_{\rm max} = 420$ kpc, the escape velocity at $r = 480$ pc is $v_{\rm esc} \sim 640$ km s^{-1}, implying that the O1 outflow is barely able to escape the central region. For the other outflow velocity values (Table 2), the ionized gas is unable to escape from the gravitational potential of the host galaxy on <500 pc scales from the nucleus, and hence cannot reach kiloparsec scales. This is also consistent with the k-plot diagnostic shown in Figure 8. As discussed in Section 3.3.10, such gas is expected to condense in situ and soon rain back toward the central SMBH via the CCA mechanism. This creates a self-regulated feeding and feedback AGN loop, which is at the core of currently consistent theoretical models (Gaspari et al. 2020, for a review).

5. Conclusions

In this work, we have presented a multiwavelength analysis of the ionized gas outflow in the nearby, radio-quiet AGN HE 0040-1105. The observations in the optical, UV, and radio have revealed multiple features that extend from galaxy scales down to <10 pc from the AGN. Our key findings are summarized as follows:

1. The ionized gas outflow in Hα is spatially unresolved by MUSE (Section 3.2.1) and confined within the central 500 pc from the nucleus (Section 3.2.2). For this region, we estimate an upper limit for the SFR (Section 3.2.4), which is exceeded by the mass outflow rate by two orders of magnitude.
2. The kiloparsec-scale ionized nebula comprises four kinematically distinct regions: (i) a central blue wing/ionized gas outflow O1, (ii) a receding ionized gas shell C1, (iii) the EELR that is local to the galaxy, and (iv) a blueshifted knot C2a on the northwest side of the nucleus (Section 3.3). Although the kinematics of the O1 outflow is nongravitational, the ionized gas motion on large scales is dominated by the bulge potential of the galaxy. The kinematic misalignment between the stars and Hα ionized gas, the quiescent EELR kinematics, and the detection of the clumpy gas in the UV is consistent with the idea that HE 0040-1105 is a late-stage merger, which can further enhance CCA condensation.
3. The flux-weighted centroids of the outflowing gas in Hα and [O III] coincide with radio emission detected in the observations acquired with the VLA and EVN (Section 3.4). Our findings suggest that the observed spatial alignment of the parsec-scale radio knots is consistent with a weak radio jet morphology, as opposed to the diffuse radio emission predicted for AGN winds (Section 4.1.3).
4. The radio spectrum of HE 0040-1105 within the frequency range of 880 MHz–10 GHz is consistent with a steep spectrum ($\alpha = -1.30 \pm 0.28$; $S_\nu \propto \nu^\alpha$). Additionally, the source demonstrates radio continuum variability on ∼20 yr timescale (Section 3.4.4).
5. The majority (∼99%) of the [O III] emission is located at the location of the flux-weighted [O III] centroid, where the estimated ionizing luminosity of the O1 outflow is similar to the mechanical power of the radio jets. However, at the outer boundary of O1, the ionizing luminosity is a factor of 2 higher than the jet power but an order of magnitude lower than the AGN bolometric luminosity. The most conclusive scenario is that the radio jets accelerate and ionize the ambient medium through the dissipation of their mechanical energy on 100 pc scales, while on galaxy scales (∼500 pc) the gas clouds interact with the photons from the AGN radiation field and are therefore photoionized (Section 4.2.2).
6. The velocity of the O1 outflow is too low to escape the host galaxy's gravitational potential from the central 500 pc, in which case the ionized clouds may rain back onto the SMBH via CCA (Section 4.3). Indeed, as tested by the k-plot diagnostic, most of the ionized clouds in HE 0040-1105 are expected to be prone to multi-phase turbulent condensation in situ (Figure 8).

Our results stress the complexity of the outflow–ISM interaction on different spatial scales, as well as the challenge

of constraining the launching mechanism of nuclear-ionized gas outflows in radio-quiet AGN. Although VLBI allowed us to tenuously resolve a jet-like morphology in the faint radio emission from HE 0040-1105, it cannot be directly identified with the galaxy-scale processes in the traced ionized gas. To distinguish between the AGN-wind versus jet launching mechanism, further multiwavelength observations are required to spatially resolve the kinematic features. Only resolving the multiphase ISM will help to understand the complex interaction between AGN and host galaxy on different spatial scales.

Acknowledgments

We thank the anonymous referee for providing useful comments that have improved the overall quality of the paper. The work of M.S. was supported in part by the University of Manitoba Graduate Enhancement of Tri-Council Stipends (GETS) program and by NASA under award number 80GSFC21M0002. The work of C.P.O. and S.A.B. was supported by a grant from the Natural Sciences and Engineering Research Council (NSERC) of Canada. M.P.T. acknowledges financial support from the State Agency for Research of the Spanish MCIU through the "Center of Excellence Severo Ochoa" award to the Instituto de Astrofísica de Andalucía (SEV-2017-0709) and through grant PID2020-117404GB-C21 (MCI/AEI/FEDER, UE). M.G. acknowledges the partial support by NASA Chandra GO9-20114X and HST GO-15890.020/023-A, and the BlackHoleWeather program. The Science and Technology Facilities Council is acknowledged by J.N. for support through the Consolidated Grant Cosmology and Astrophysics at Portsmouth, ST/S000550/1.

The EVN is a joint facility of independent European, African, Asian, and North American radio astronomy institutes. Scientific results from data presented in this publication are derived from the following EVN project code: EP119 (PI: Pérez Torres). e-VLBI research infrastructure in Europe is supported by the European Union's Seventh Framework Program (FP7/2007-2013) under grant agreement number RI-261525 NEXPReS. The National Radio Astronomy Observatory is a facility of the National Science Foundation operated under cooperative agreement by Associated Universities, Inc.

Facilities: EVN, VLA, VLT:Yepun (MUSE).

Software: Astropy (Astropy Collaboration et al. 2013, 2018), CASA (McMullin et al. 2007), AIPS (Wells 1985), Matplotlib (Hunter 2007), NumPy (van der Walt et al. 2011), SciPy (Virtanen et al. 2020), VorBin (Cappellari & Copin 2003).

Appendix A
Fitting Multicomponent Emission Line Spectra in the Hα Window

In Sections 3.3.4 and 3.3.7, we spectroscopically deblended the red-wing components of both features C1 and C2 in both the [O III] and Hα windows. While we have only shown the spectral fit for the Hβ + [O III] emission lines, the BPT diagnostic also requires the emission line fluxes of Hα and [N II]. Since the lines consist of multiple components, we also show their spectra and the best-fit models here in Figure 13. Similar to the modeling of the Hβ and [O III] emission lines shown in Figure 6, we extract the same 3 × 3 spaxel aperture spectrum around the Hα + [N II] + [S II] emission line complex and fit it with a two-component model. The second component is only employed if the AIC criterion described in Section 3.2.1 is fulfilled.

We model the 9 × 9 spaxel aperture spectrum around C2 (see Figure 7) in the Hα window in a similar fashion as that used for C1.

In both cases, C1 and C2, two components are required to reproduce the emission line shape. In the C1 aperture spectrum, the core component corresponds to the EELR local to the galaxy, whereas the red wing belongs to the kinematically distinct feature C1 (denoted by the brown Gaussian components). For the C2 aperture spectrum, the blue and the green Gaussian components correspond to C2a and C2b, respectively. Combining the best-fit results with what we have retrieved in the Hβ + [O III] window, the BPT characterizations of C1, C2a, and C2b are shown in Figure 12.

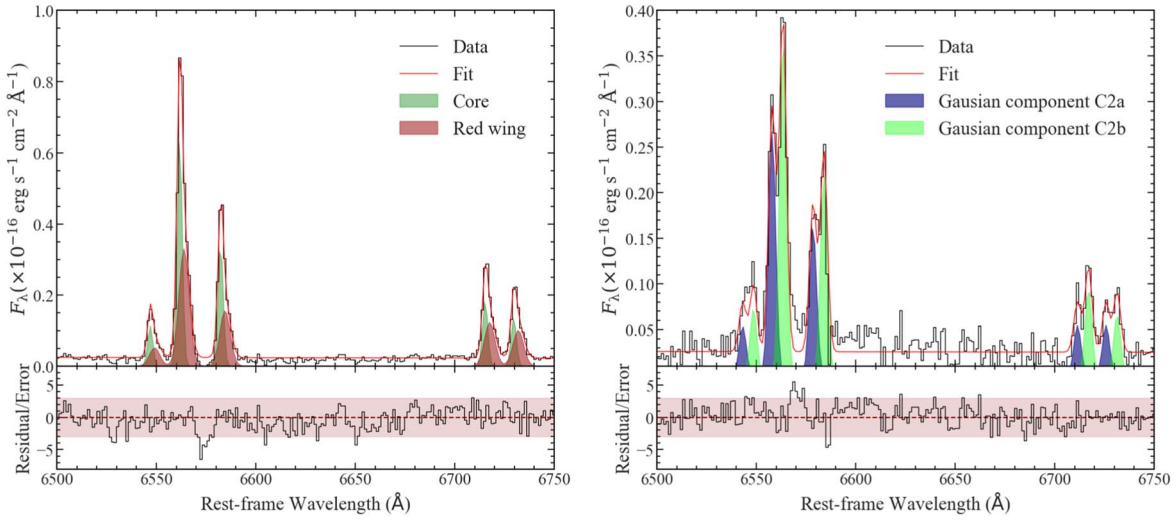

Figure 13. Similar to the left panel of Figure 6, the left panel here shows the 3 × 3 spaxel aperture spectra extracted from C1 and their two-component modeling. The figure organization and symbols are similar to Figure 6 (left panel). The right panel shows the 9 × 9 spaxel aperture spectra extracted at the location of C2 together with the best-fit two-component model and the emission line spectra of the individual components. The figure organization and symbols are similar to the upper left panel of Figure 7.

Appendix B
Constraining the Morphology of the Ionized Gas Cloud C1

In Section 3.3.3, we identified a spatially resolved, redshifted ionized gas cloud C1 that is located east of the AGN. Here we describe how we constrain the underlying morphology. As a first step, we map the surface brightness profile of the emission line component, which is shown in the left panel of Figure 14. The red wing component's signal is blended with the bright blue wing component. The AIC criterion described in Section 3.2.1 therefore introduces an artificial cutoff close to the nucleus, which is not physical. Since the peak of the surface brightness profile is clearly visible and offset from the AGN position, we exclusively concentrate on the eastward extension of the profile for the following analysis. Since C1 appears to be elongated in the north–south direction, we first extract the 1D flux of the source at fixed decl. As a next step, we estimate the width of the source by fitting the profile with a one-dimensional Gaussian profile, for every slice extracted. In order to account for beam smearing, we convolve the Gaussian profile with the PSF before minimizing the χ^2 residuals, which provides us with both the location and the intrinsic extent of the feature. The bottom right panel of Figure 14 shows that the location of C1's maximum luminosity is almost constant, which we interpret as a shell-like morphology. The shell is located 600 pc distance away from the nucleus. Its median width in the east–west direction is 255 pc.

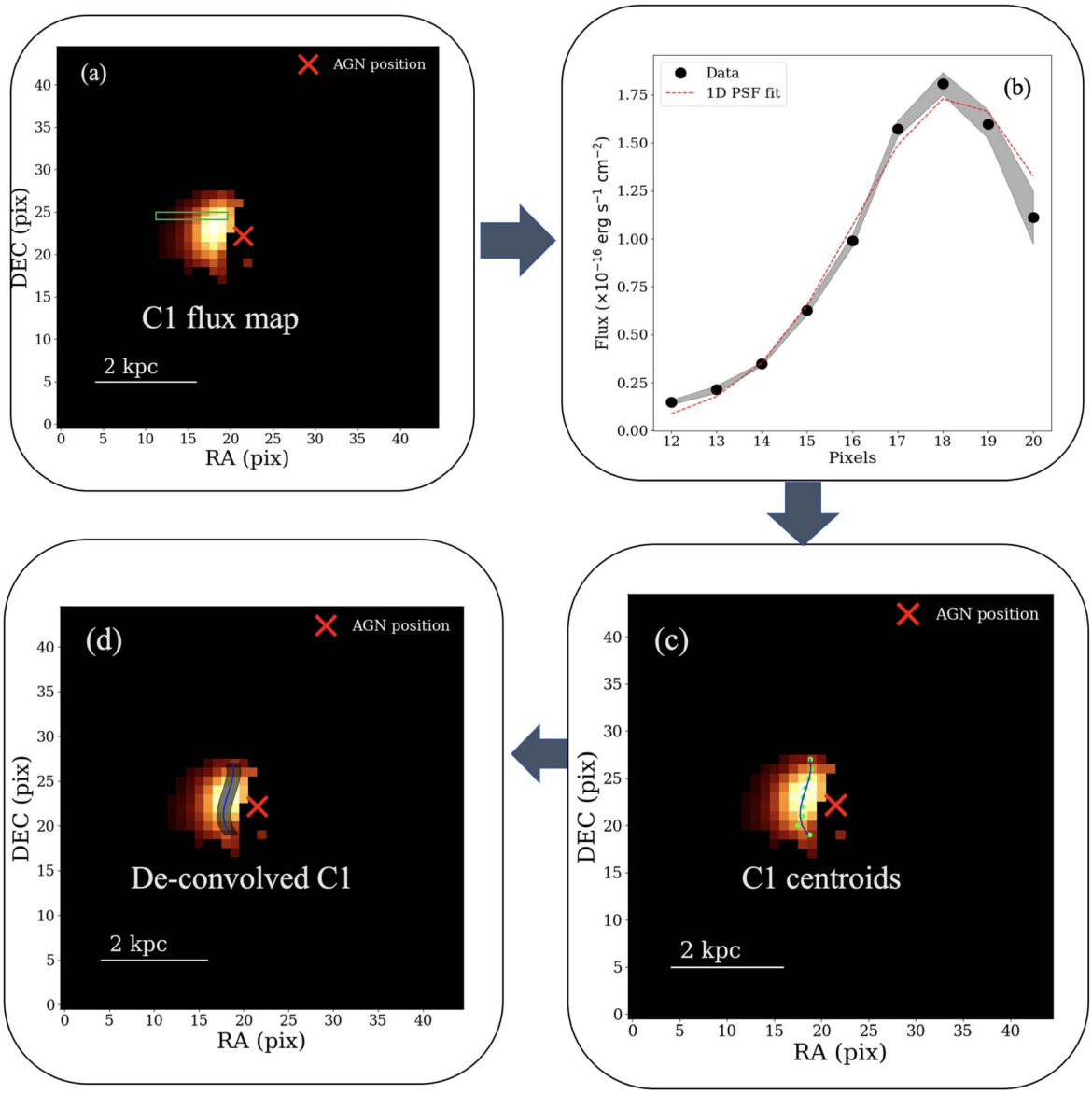

Figure 14. Flowchart showing the method by which we constrain the location and morphology of the ionized gas cloud C1. Panel (a) shows the flux map retrieved from the two-component model fitted to the original MUSE data cube. In panel (b), we show an example slice of the flux profile at fixed decl., together with the model of the PSF. This slice has been taken from the slice at the decl. with the brightest C1 emission, where the 1D PSF fit follows the 1D flux profile closely. We map the location of the one-dimensional surface profiles in panel (c), which line up to a shell that extends in the north–south direction. The blue line represents the centroids of C1. Panel (d) shows the deconvolved image of C1, where the width of the underlying structure is achieved by fitting with the flux profile at a fixed decl. with the brightest C1 emission with a 1D PSF convolved with a 1D Gaussian. The standard deviation of the Gaussian provides us with the width of the structure (shaded in gray).

ORCID iDs

M. Singha https://orcid.org/0000-0001-5687-1516
N. Winkel https://orcid.org/0000-0001-9428-6238
S. Vaddi https://orcid.org/0000-0003-3295-6595
M. Perez Torres https://orcid.org/0000-0001-5654-0266
M. Gaspari https://orcid.org/0000-0003-2754-9258
I. Smirnova-Pinchukova https://orcid.org/0000-0002-2260-3043
C. P. O'Dea https://orcid.org/0000-0001-6421-054X
F. Combes https://orcid.org/0000-0003-2658-7893
T. Rose https://orcid.org/0000-0002-8310-2218
R. McElroy https://orcid.org/0000-0002-7960-5808
B. Husemann https://orcid.org/0000-0003-2901-6842
T. A. Davis https://orcid.org/0000-0003-4932-9379
S. A. Baum https://orcid.org/0000-0002-4735-8224
C. Lawlor-Forsyth https://orcid.org/0000-0002-2958-0593
J. Neumann https://orcid.org/0000-0002-3289-8914
G. R. Tremblay https://orcid.org/0000-0002-5445-5401

References

Aalto, S., Muller, S., Costagliola, F., et al. 2017, A&A, 608, A22
Agudo, I., Boettcher, M., Falcke, H. D. E., et al. 2015, in Advancing Astrophysics with the Square Kilometre Array (AASKA14) (Trieste: SISSA), 93
Akaike, H. 1974, ITAC, 19, 716
Arata, S., Yajima, H., & Nagamine, K. 2018, MNRAS, 475, 4252
Astropy Collaboration, Price-Whelan, A. M., Sipőcz, B. M., et al. 2018, AJ, 156, 123
Astropy Collaboration, Robitaille, T. P., Tollerud, E. J., et al. 2013, A&A, 558, A33
Baldwin, J. A., Phillips, M. M., & Terlevich, R. 1981, PASP, 93, 5
Baron, D., & Netzer, H. 2019, MNRAS, 482, 3915
Barrera-Ballesteros, J. K., García-Lorenzo, B., Falcón-Barroso, J., et al. 2015, A&A, 582, A21
Barvainis, R., Lehár, J., Birkinshaw, M., Falcke, H., & Blundell, K. M. 2005, ApJ, 618, 108
Baum, S. A., O'Dea, C. P., Giovannini, G., et al. 1997, ApJ, 483, 178
Becker, R. H., White, R. L., & Helfand, D. J. 1995, ApJ, 450, 559
Benson, A. J., Bower, R. G., Frenk, C. S., et al. 2003, ApJ, 599, 38
Berton, M., Järvelä, E., Crepaldi, L., et al. 2020, A&A, 636, A64
Bian, W., Gu, Q., Zhao, Y., Chao, L., & Cui, Q. 2006, MNRAS, 372, 876
Bischetti, M., Piconcelli, E., Vietri, G., et al. 2017, A&A, 598, A122
Blundell, K. M., & Beasley, A. J. 1998, MNRAS, 299, 165
Bower, R. G., Benson, A. J., Malbon, R., et al. 2006, MNRAS, 370, 645
Brunthaler, A., Falcke, H., Bower, G. C., et al. 2000, A&A, 357, L45
Calzetti, D., Kennicutt, R. C., Engelbracht, C. W., et al. 2007, ApJ, 666, 870
Cano-Díaz, M., Maiolino, R., Marconi, A., et al. 2012, A&A, 537, L8
Cappellari, M., & Copin, Y. 2003, MNRAS, 342, 345
Cardelli, J. A., Clayton, G. C., & Mathis, J. S. 1989, ApJ, 345, 245
Cavagnolo, K. W., McNamara, B. R., Nulsen, P. E. J., et al. 2010, ApJ, 720, 1066
Cicone, C., Brusa, M., Ramos Almeida, C., et al. 2018, NatAs, 2, 176
Crenshaw, D. M., Fischer, T. C., Kraemer, S. B., & Schmitt, H. R. 2015, ApJ, 799, 83
Crenshaw, D. M., & Kraemer, S. B. 2012, ApJ, 753, 75
Cresci, G., Marconi, A., Zibetti, S., et al. 2015, A&A, 582, A63
Cypriano, E. S., Amara, A., Voigt, L. M., et al. 2010, MNRAS, 405, 494
Davis, T. A., Alatalo, K., Bureau, M., et al. 2013, MNRAS, 429, 534
Davis, T. A., Alatalo, K., Sarzi, M., et al. 2011, MNRAS, 417, 882
Diniz, M. R., Riffel, R. A., Storchi-Bergmann, T., & Winge, C. 2015, MNRAS, 453, 1727
Elvis, M. 2000, ApJ, 545, 63
Emonts, B. H. C., Morganti, R., Tadhunter, C. N., et al. 2005, MNRAS, 362, 931
Eriksen, M., & Hoekstra, H. 2018, MNRAS, 477, 3433
Fabian, A. 2012, ARA&A, 50, 455
Falcke, H., Lehár, J., Barvainis, R., Nagar, N. M., & Wilson, A. S. 2001, in ASP Conf. Ser. 224, Probing the Physics of Active Galactic Nuclei, ed. B. M. Peterson, R. W. Pogge, & R. S. Polidan (San Francisco, CA: ASP), 265
Faucher-Giguère, C.-A., & Quataert, E. 2012, MNRAS, 425, 605
Fiore, F., Feruglio, C., Shankar, F., et al. 2017, A&A, 601, A143
Gallimore, J. F., Axon, D. J., O'Dea, C. P., Baum, S. A., & Pedlar, A. 2006, AJ, 132, 546
Gaspari, M., Brighenti, F., D'Ercole, A., & Melioli, C. 2011, MNRAS, 411, 349
Gaspari, M., Eckert, D., Ettori, S., et al. 2019, ApJ, 884, 169
Gaspari, M., McDonald, M., Hamer, S. L., et al. 2018, ApJ, 854, 167
Gaspari, M., Ruszkowski, M., & Oh, S. P. 2013, MNRAS, 432, 3401
Gaspari, M., & Sądowski, A. 2017, ApJ, 837, 149
Gaspari, M., Tombesi, F., & Cappi, M. 2020, NatAs, 4, 10
Girdhar, A., Harrison, C. M., Mainieri, V., et al. 2022, MNRAS, 512, 1608
Gonzaga, S., Hack, W., Fruchter, A., & Mack, J. 2012, The DrizzlePac Handbook (Baltimore: STScI), 291
Green, R. F., Schmidt, M., & Liebert, J. 1986, ApJS, 61, 305
Greene, J. E., & Ho, L. C. 2005, ApJ, 627, 721
Greene, J. E., Zakamska, N. L., Ho, L. C., & Barth, A. J. 2011, ApJ, 732, 9
Güdel, M., & Benz, A. O. 1993, ApJL, 405, L63
Güver, T., & Özel, F. 2009, MNRAS, 400, 2050
Hardcastle, M. J., & Croston, J. H. 2020, NewAR, 88, 101539
Harrison, C. M., Alexander, D. M., Mullaney, J. R., & Swinbank, A. M. 2014, MNRAS, 441, 3306
Harrison, C. M., Thomson, A. P., Alexander, D. M., et al. 2015, ApJ, 800, 45
Herrera-Camus, R., Tacconi, L., Genzel, R., et al. 2019, ApJ, 871, 37
Holt, J., Tadhunter, C. N., & Morganti, R. 2008, MNRAS, 387, 639
Hopkins, P. F., & Elvis, M. 2010, MNRAS, 401, 7
Huang, K.-H., Fall, S. M., Ferguson, H. C., et al. 2017, ApJ, 838, 6
Huchra, J., & Burg, R. 1992, ApJ, 393, 90
Hunter, J. D. 2007, CSE, 9, 90
Husemann, B., Scharwächter, J., Bennert, V. N., et al. 2016, A&A, 594, A44
Husemann, B., Scharwächter, J., Davis, T. A., et al. 2019, A&A, 627, A53
Husemann, B., Singha, M., Scharwächter, J., et al. 2022, A&A, 659, A124
Husemann, B., Tremblay, G., Davis, T., et al. 2017, Msngr, 169, 42
Jaffarian, G. W., & Gaskell, C. M. 2020, MNRAS, 493, 930
Jarvis, M. E., Harrison, C. M., Thomson, A. P., et al. 2019, MNRAS, 485, 2710
Jin, Y., Chen, Y., Shi, Y., et al. 2016, MNRAS, 463, 913
King, A. 2003, ApJL, 596, L27
King, A. 2005, ApJL, 635, L121
Kormendy, J., & Ho, L. C. 2013, ARA&A, 51, 511
Lacy, M., Baum, S. A., Chandler, C. J., et al. 2020, PASP, 132, 035001
Laing, R. A., & Bridle, A. H. 2014, MNRAS, 437, 3405
Laor, A., & Behar, E. 2008, MNRAS, 390, 847
Lau, E. T., Gaspari, M., Nagai, D., & Coppi, P. 2017, ApJ, 849, 54
Liu, Y., Wang, R., Momjian, E., et al. 2022, ApJL, 939, L5
Maccagni, F. M., Serra, P., Gaspari, M., et al. 2021, A&A, 656, A45
Mahony, E. K., Oonk, J. B. R., Morganti, R., et al. 2016, MNRAS, 455, 2453
McCarthy, I. G., Schaye, J., Ponman, T. J., et al. 2010, MNRAS, 406, 822
McElroy, R., Croom, S. M., Pracy, M., et al. 2015, MNRAS, 446, 2186
McElroy, R., Singha, M., Husemann, B., et al. 2022, Msngr, 187, 3
McMullin, J. P., Waters, B., Schiebel, D., Young, W., & Golap, K. 2007, in ASP Conf. Ser. 376, Astronomical Data Analysis Software and Systems XVI, ed. R. A. Shaw, F. Hill, & D. J. Bell (San Francisco, CA: ASP), 127
McNamara, B. R., & Nulsen, P. E. 2012, NJPh, 14, 055023
Miller, P., Rawlings, S., & Saunders, R. 1993, MNRAS, 263, 425
Moll, R., Schindler, S., Domainko, W., et al. 2007, A&A, 463, 513
Molyneux, S. J., Harrison, C. M., & Jarvis, M. E. 2019, A&A, 631, A132
Morganti, R., Fogasy, J., Paragi, Z., Oosterloo, T., & Orienti, M. 2013, Sci, 341, 1082
Mullaney, J. R., Alexander, D. M., Fine, S., et al. 2013, MNRAS, 433, 622
Mundell, C. G., Ferruit, P., Nagar, N., & Wilson, A. S. 2009, ApJ, 703, 802
Muratov, A. L., Kereš, D., Faucher-Giguère, C.-A., et al. 2015, MNRAS, 454, 2691
Murphy, E. J., Condon, J. J., Schinnerer, E., et al. 2011, ApJ, 737, 67
Nagar, N. M., Falcke, H., Wilson, A. S., & Ulvesta, J. S. 2002, A&A, 392, 53
Nelson, C. H., & Whittle, M. 1996, ApJ, 465, 96
North, E. V., Davis, T. A., Bureau, M., et al. 2021, MNRAS, 503, 5179
Oppenheimer, B. D., Davé, R., Kereš, D., et al. 2010, MNRAS, 406, 2325
Panessa, F., Baldi, R. D., Laor, A., et al. 2019, NatAs, 3, 387
Panessa, F., Pérez-Torres, M., Hernández-García, L., et al. 2022, MNRAS, 510, 718
Proga, D. 2007, in ASP Conf. Ser. 373, The Central Engine of Active Galactic Nuclei, ed. L. C. Ho & J. W. Wang (San Francisco, CA: ASP), 267
Rakshit, S., & Woo, J.-H. 2018, ApJ, 865, 5
Rupke, D. S., & Veilleux, S. 2013, ApJ, 768, 75
Rupke, D. S., Veilleux, S., & Sanders, D. B. 2002, ApJ, 570, 588

Sahu, K. 2021, WFC3 Data Handbook, Version 5.0 (Baltimore: STScI), 289
Schaye, J., Crain, R. A., Bower, R. G., et al. 2015, MNRAS, 446, 521
Schindler, S., & Diaferio, A. 2008, SSRv, 134, 363
Schulz, R., Morganti, R., Nyland, K., et al. 2018, A&A, 617, A38
Silk, J., & Rees, M. J. 1998, A&A, 331, L1
Singha, M., O'Dea, C. P., & Baum, S. A. 2023, Galax, 11, 85
Singha, M., O'Dea, C. P., Gordon, Y. A., Lawlor-Forsyth, C., & Baum, S. A. 2021a, ApJ, 918, 65
Singha, M., Husemann, B., Urrutia, T., et al. 2022, A&A, 659, A123
Smirnova-Pinchukova, I., Husemann, B., Davis, T. A., et al. 2022, A&A, 659, A125
Storey, P. J., & Zeippen, C. J. 2000, MNRAS, 312, 813
Sun, M., Xue, Y., Trump, J. R., & Gu, W.-M. 2019, MNRAS, 482, 2788
Tadhunter, C., Marconi, A., Axon, D., et al. 2003, MNRAS, 342, 861
Takeuchi, S., Ohsuga, K., & Mineshige, S. 2013, PASJ, 65, 88
Temi, P., Gaspari, M., Brighenti, F., et al. 2022, ApJ, 928, 150
Thean, A. H. C., Gillibrand, T. I., Pedlar, A., & Kukula, M. J. 2001, MNRAS, 327, 369
Tremblay, G. R., Oonk, J. B. R., Combes, F., et al. 2016, Natur, 534, 218
U, V., Lai, T., Bianchin, M., et al. 2022, ApJL, 940, L5
Ulvestad, J. S., Antonucci, R. R. J., & Barvainis, R. 2005, ApJ, 621, 123
van der Walt, S., Colbert, S. C., & Varoquaux, G. 2011, CSE, 13, 22
Villar-Martín, M., Emonts, B., Cabrera Lavers, A., et al. 2017, MNRAS, 472, 4659
Virtanen, P., Gommers, R., Oliphant, T. E., et al. 2020, NatMe, 17, 261
Weilbacher, P. M., Palsa, R., Streicher, O., et al. 2020, A&A, 641, A28
Wells, D. C. 1985, in Data Analysis in Astronomy, ed. V. Di Gesù et al. (New York: Plenum), 195
Whittle, M. 1992, ApJ, 387, 109
Wilkins, D. R., Gallo, L. C., Costantini, E., Brandt, W. N., & Blandford, R. D. 2021, Natur, 595, 657
Winkel, N., Husemann, B., Davis, T. A., et al. 2022, A&A, 663, A104
Winkel, N., Husemann, B., Singha, M., et al. 2023, A&A, 670, A3
Wisotzki, L., Christlieb, N., Bade, N., et al. 2000, A&A, 358, 77
Wittor, D., & Gaspari, M. 2020, MNRAS, 498, 4983
Woo, J.-H., Bae, H.-J., Son, D., & Karouzos, M. 2016, ApJ, 817, 108
Zakamska, N. L., & Greene, J. E. 2014, MNRAS, 442, 784
Zubovas, K., & Bourne, M. A. 2017, MNRAS, 468, 4956